ELSEVIER

Comput. Methods Appl. Mech. Engrg. 191 (2002) 2949–2978

Computer methods in applied mechanics and engineering

www.elsevier.com/locate/cma

Finite element simulation of strain localization with large deformation: capturing strong discontinuity using a Petrov–Galerkin multiscale formulation

Ronaldo I. Borja

Department of Civil and Environmental Engineering, Terman Building, Stanford University, Stanford, CA 94305-4020, USA

Received 13 August 2001; received in revised form 4 December 2001

Abstract

The finite element model for strain localization analysis developed in a previous work is generalized to the finite deformation regime. Strain enhancements via jumps in the displacement field are captured and condensed on the material level, leading to a formulation that does not require static condensation to be performed on the element level. A general evolution condition is first formulated laying out conditions for the continued activation of a strong discontinuity. Then, a multiscale finite element model is formulated to describe the post-bifurcation behavior, highlighting the key roles played by the continuous and conforming deformation maps on the characterization of the finite deformation kinematics of a localized element traced by a strong discontinuity. The resulting finite element equation exhibits the features of a Petrov–Galerkin formulation in which the gradient of the weighting function is evaluated over the continuous part of the deformation map, whereas the gradient of the trial function is evaluated over the conforming part of the same map. In the limit of infinitesimal deformations the formulation reduces to the standard Galerkin approximation described in a previous work. Numerical examples are presented demonstrating absolute objectivity with respect to mesh refinement and insensitivity to mesh alignment of finite element solutions.

1. Introduction

Strain localization involves the development of a very narrow zone, or band, in a solid continuum inside which the deformation is intense and the material strength and stiffness have degraded significantly from those prevailing outside this zone. Factors responsible for localized deformation include initial imperfections and defects in the continuum, non-uniform loading, and boundary constraints, among others [1–6]. Simulations of strain localization incorporating these factors are prohibitively expensive if not impossible, leading the analyst to consider the phenomena from the point of view of material instability where the localized deformation is triggered by a bifurcation from a homogeneous material behavior [7–13]. Such

E-mail address: borja@stanford.edu (R.I. Borja).

0045-7825/02/$ - see front matter
PII: S0045-7825(02)00218-9

instability, as well as the accompanying nonhomogeneous deformation, are influenced to a great extent by geometric nonlinearities particularly during the advanced stages of loading [14–18].

Capturing strain localization phenomena using finite element analysis requires a careful treatment of both the microscale and macroscale fields [19–22]. Such treatment is not limited to the kinematical description of deformation alone but may also include characterization of the bifurcated constitutive response inside the localization band [23–27]. An example of a bifurcated constitutive response is the accelerated softening behavior exhibited by the granular material inside a crack or fault as compared to that exhibited by the parent rock [28]. In bulk metallic glasses, the localization zone also exhibits an increase in the production of free volumes not exhibited by the intact glass [29]. Incorporating these behavioral patterns as well as the accompanying finite deformation effects into the microscale and macroscale fields is a challenging task for the analyst.

A majority of research effort in shear band mode bifurcation analysis has focused primarily on the geometrically linear case. In general, any result derived from such analysis must be taken with caution since geometric nonlinearities play a very crucial role in the theory of bifurcation. A recent paper shows that finite deformation effects do enhance strain localization, and that bifurcation is possible even in the hardening regime of an associative plasticity model [30]. This suggests that ignoring geometric nonlinearities is not conservative, and efforts to systematically include these effects both in the bifurcation and post-bifurcation analyses must be supported whenever possible. To this end, significant strides have been made in [31,32] to include large deformation effects in strain localization analysis, but progress in the development of more efficient, accurate, and robust procedures remains limited.

The assumed enhanced strain (AES) formulation proposed in [33] is the most common basis of finite element simulation of strain localization phenomena. With a suitable choice of the weighting function for the enhanced field, it provides a general mathematical framework that circumvents the problem of mesh-dependence afflicting the standard finite element formulation [25,26,31,32,34–36]. However, this approach does not allow a unique definition of the enhanced weighting function. In general, there is a host of such weighting functions that pass the so-called patch test [37], each one predicting a different post-localized response that is not readily amenable to physical interpretation. Furthermore, the static condensation technique required by the method is unwieldy and tricky, particularly when the enhanced weighting function and the post-localized behavior vary nonlinearly with the slip degree of freedom being condensed.

A recent work has utilized the standard Galerkin procedure for casting the strain localization problem within the framework of finite element method with embedded strong discontinuity [24]. The method was shown to be equivalent to the AES formulation for the case of piecewise constant stresses and strains provided by the constant strain triangle (CST) interpolation. More importantly, the formulation identifies the auxiliary equation for the enhanced strain field as nothing more than the consistency condition that must be satisfied on the band, as well as uniquely defines the auxiliary weighting function as the gradient of the yield function on the band. This approach thus allows the predicted post-localized behavior to be interpreted in a more meaningful fashion. Furthermore, the tricky and undesirable static condensation technique inherent in the AES method has been eliminated completely in the solution procedure.

The objective of this paper is to generalize the solution procedure proposed in [24] to the finite deformation regime. To this end, we first derive conditions for the evolution of a preexisting band, and for the case of strong discontinuity this requires that the objective jump velocity vector be tangent to the band. Then, we formulate a multiscale finite element model to capture strong discontinuity in a finite deformation setting. In order to preserve the sparse structure of the overall coefficient matrix, the global linear momentum balance is formulated spatially. Since the symmetric Kirchhoff (true) stress tensor is related to the non-symmetric first Piola–Kirchhoff stress tensor through the deformation gradient of the continuous part of motion, the gradient of the standard weighting function is evaluated over the so-called continuous deformation map. In contrast, the Kirchhoff stress tensor is formulated over the conforming deformation

map, leading to a Petrov–Galerkin finite element formulation. In the limit of infinitesimal deformation, or in the limit of zero displacement jump for the case of finite deformation, the standard Galerkin approximation is recovered naturally from the formulation.

As for notations and symbols, bold-face letters denote matrices and vectors; the symbol '·' denotes an inner product of two vectors (e.g. $\boldsymbol{a}\cdot\boldsymbol{b}=a_ib_i$), or a single contraction of adjacent indices of two tensors (e.g. $\boldsymbol{c}\cdot\boldsymbol{d}=c_{ij}d_{jk}$); the symbol ':' denotes an inner product of two second-order tensors (e.g. $\boldsymbol{c}:\boldsymbol{d}=c_{ij}d_{ij}$), or a double contraction of adjacent indices of tensors of rank two and higher (e.g. $\boldsymbol{C}:\boldsymbol{\epsilon}^{\mathrm{e}}=C_{ijkl}\epsilon^{\mathrm{e}}_{kl}$). We also adopt the following general tensor notations: $\boldsymbol{P}$, non-symmetric first Piola–Kirchhoff stress; $\boldsymbol{S}$, symmetric second Piola–Kirchhoff stress; $\boldsymbol{\tau}$, symmetric Kirchhoff (true) stress; $\boldsymbol{\sigma}$, symmetric Cauchy stress; $\boldsymbol{F}$, deformation gradient with respect to the undeformed configuration; $\boldsymbol{f}$, relative deformation gradient; $\boldsymbol{b}$, left Cauchy–Green deformation, and $\boldsymbol{l}$, spatial velocity gradient. Tangent operators are defined as they appear in the text.

2. Formulation of microscale model

In this section we present a continuum formulation of the microscale model as well as develop necessary conditions for the shear band to evolve in the localized state.

2.1. Shear band kinematics

Consider a shear band whose deformation is described by the ramp-like relation

$$\boldsymbol{\phi}=\begin{cases}\bar{\boldsymbol{\phi}}, & \text{if } \kappa\leqslant 0;\\ \bar{\boldsymbol{\phi}}+\kappa[\![\boldsymbol{\phi}]\!]/h_0, & \text{if } 0\leqslant\kappa\leqslant h_0;\\ \bar{\boldsymbol{\phi}}+[\![\boldsymbol{\phi}]\!], & \text{if } \kappa\geqslant h_0,\end{cases}\tag{2.1}$$

where $\bar{\boldsymbol{\phi}}=\bar{\boldsymbol{\phi}}(X)$ is a continuous deformation field, $[\![\boldsymbol{\phi}]\!]$ is the relative deformation of one side $\hat{\mathscr{S}}_0$ of the band with respect to the other side $\mathscr{S}_0$, and h_0 is the thickness of the shear band in the reference configuration. The variable κ is a normal parameter given by the relation

$$\kappa=(\boldsymbol{X}-\boldsymbol{Y})\cdot\boldsymbol{N},\tag{2.2}$$

where $\boldsymbol{Y}$ is any point on $\mathscr{S}_0$ whose unit normal is $\boldsymbol{N}$. The associated deformation gradient is obtained as

$$\boldsymbol{F}=\frac{\partial\boldsymbol{\phi}}{\partial\boldsymbol{X}}=\begin{cases}\overline{\boldsymbol{F}} & \text{in } \mathscr{B}\setminus\overline{\mathscr{D}}_0;\\ \overline{\boldsymbol{F}}+([\![\boldsymbol{\phi}]\!]\otimes\boldsymbol{N})/h_0 & \text{in } \mathscr{D}_0,\end{cases}\tag{2.3}$$

where $\overline{\boldsymbol{F}}=\partial\bar{\boldsymbol{\phi}}/\partial\boldsymbol{X}$, and $\overline{\mathscr{D}}_0=\mathscr{S}_0\times[0,h_0]$ is the shear band domain. Throughout the formulation we shall assume that the jumps $[\![\boldsymbol{\phi}]\!]$ and $[\![\dot{\boldsymbol{\phi}}]\!]$ are spatially constant on $\mathscr{S}_0$ (in finite element analysis, the spatial constancy of the jump vectors applies only to each finite element, but they may be discontinuous across the element boundaries).

Next, consider the following ramp-like description of velocity field in the same continuum

$$\boldsymbol{V}(X)=\begin{cases}\overline{\boldsymbol{V}} & \text{if } \kappa\leqslant 0;\\ \overline{\boldsymbol{V}}+\kappa[\![\boldsymbol{V}]\!]/h_0 & \text{if } 0\leqslant\kappa\leqslant h_0;\\ \overline{\boldsymbol{V}}+[\![\boldsymbol{V}]\!] & \text{if } \kappa\geqslant h_0,\end{cases}\tag{2.4}$$

where $\overline{\boldsymbol{V}}=\dot{\bar{\boldsymbol{\phi}}}(X)$ is the continuous velocity field, and $[\![\boldsymbol{V}]\!]=[\![\dot{\boldsymbol{\phi}}]\!]$ is the relative velocity of $\hat{\mathscr{S}}_0$ to $\mathscr{S}_0$ induced by the shear band deformation. We recall that the material velocity $\boldsymbol{V}(X)$ of point X is equal to the spatial

velocity $\boldsymbol{v}(x)$ of point x if the spatial point x is the same material point X in the reference configuration. The time derivatives of $\boldsymbol{F}$ then take the form

$$\dot{\boldsymbol{F}} = \begin{cases} \dot{\overline{\boldsymbol{F}}} & \text{in } \mathscr{B} \setminus \overline{\mathscr{D}}_0; \\ \dot{\overline{\boldsymbol{F}}} + (\llbracket \boldsymbol{V} \rrbracket \otimes \boldsymbol{N})/h_0 & \text{in } \mathscr{D}_0, \end{cases} \tag{2.5}$$

where $\dot{\boldsymbol{F}} = \partial \boldsymbol{V}/\partial \boldsymbol{X}$ and $\dot{\overline{\boldsymbol{F}}} = \partial \overline{\boldsymbol{V}}/\partial \boldsymbol{X}$.

The corresponding expressions for the spatial velocity gradient $\boldsymbol{l} = \dot{\boldsymbol{F}} \cdot \boldsymbol{F}^{-1}$ can be derived with the aid of the Sherman–Morrison formula for the inverse of $\boldsymbol{F}$ as

$$\boldsymbol{F}^{-1} = \begin{cases} \overline{\boldsymbol{F}}^{-1} & \text{in } \mathscr{B} \setminus \overline{\mathscr{D}}_0; \\ \overline{\boldsymbol{F}}^{-1} - (\boldsymbol{\Phi} \otimes \boldsymbol{N} \cdot \overline{\boldsymbol{F}}^{-1})/(h_0 + \boldsymbol{N} \cdot \boldsymbol{\Phi}) & \text{in } \mathscr{D}_0, \end{cases} \tag{2.6}$$

where $\boldsymbol{\Phi} = \overline{\boldsymbol{F}}^{-1} \cdot \llbracket \boldsymbol{\phi} \rrbracket$ is a pull-back of the jump $\llbracket \boldsymbol{\phi} \rrbracket$. The final forms for $\boldsymbol{l}$ are then given by

$$\boldsymbol{l} = \begin{cases} \bar{\boldsymbol{l}} & \text{in } \mathscr{B} \setminus \overline{\mathscr{D}}_0; \\ \bar{\boldsymbol{l}} + (\overset{\nabla}{\llbracket \boldsymbol{\phi} \rrbracket} \otimes \boldsymbol{n})/h & \text{in } \mathscr{D}_0, \end{cases} \tag{2.7}$$

where h is the current thickness of the shear band, $\boldsymbol{n}$ is the unit normal vector to the shear band in the current configuration, and

$$\bar{\boldsymbol{l}} = \dot{\overline{\boldsymbol{F}}} \cdot \overline{\boldsymbol{F}}^{-1}, \quad \overset{\nabla}{\llbracket \boldsymbol{\phi} \rrbracket} = \llbracket \dot{\boldsymbol{\phi}} \rrbracket - \bar{\boldsymbol{l}} \cdot \llbracket \boldsymbol{\phi} \rrbracket. \tag{2.8}$$

At the onset of localization, $\llbracket \boldsymbol{\phi} \rrbracket = \boldsymbol{0}$ and $\overset{\nabla}{\llbracket \boldsymbol{\phi} \rrbracket} = \llbracket \dot{\boldsymbol{\phi}} \rrbracket$; however, in the post-localized regime where $\llbracket \boldsymbol{\phi} \rrbracket \neq \boldsymbol{0}$ the jump rate $\overset{\nabla}{\llbracket \boldsymbol{\phi} \rrbracket}$ contains a convected part, which makes it an objective jump rate co-rotational with the cumulative displacement jump $\llbracket \boldsymbol{\phi} \rrbracket$, see [32].

The shear band kinematics presented above allows an evaluation of the evolution of the shear band thickness h as a function of the original thickness h_0. Nanson's formula states that $\boldsymbol{n}\,\mathrm{d}a = J\boldsymbol{F}^{-t} \cdot \boldsymbol{N}\,\mathrm{d}A$, where $\mathrm{d}a$ and $\mathrm{d}A$ are infinitesimal surface areas whose unit normals are $\boldsymbol{n}$ and $\boldsymbol{N}$, respectively, and J is the Jacobian [38]. Let $\mathrm{d}v = h\,\mathrm{d}a$, $\mathrm{d}V = h_0\,\mathrm{d}A$, and note that $J = \mathrm{d}v/\mathrm{d}V$ and $(\boldsymbol{F}^{-t} \cdot \boldsymbol{N})_i = (\boldsymbol{N} \cdot \boldsymbol{F}^{-1})_i$. Inserting these into the above formula, we get

$$\frac{\boldsymbol{n}}{h} = \frac{\boldsymbol{N} \cdot \boldsymbol{F}^{-1}}{h_0} = \frac{\boldsymbol{N} \cdot \overline{\boldsymbol{F}}^{-1}}{h_0 + \boldsymbol{N} \cdot \boldsymbol{\Phi}}. \tag{2.9}$$

The above relation is the same as Eq. (29) of [32]. However, it must be noted that this relationship holds only for the special case where the displacement varies across the band in a ramp-like fashion. For other, nonlinear continuous functions that tend to the Heaviside function in the limit of zero shear band thickness, the above relationship between h and h_0 generally does not hold.

The above relations follow the normal transformation of the elements of the cotangent space. Note, however, that the direction of $\boldsymbol{n}$ is affected only by the continuous part $\overline{\boldsymbol{F}}^{-1}$, and that the discontinuous part of $\boldsymbol{F}^{-1}$ simply serves to scale the magnitudes of the relevant vectors. Solving for h and utilizing once again the expression for $\boldsymbol{F}$ inside the shear band gives

$$h = h_0 \boldsymbol{n} \cdot \overline{\boldsymbol{F}} \cdot \boldsymbol{N} + \boldsymbol{n} \cdot \llbracket \boldsymbol{\phi} \rrbracket. \tag{2.10}$$

The first term on the right-hand side represents the evolution of the shear band thickness induced by the continuous part of deformation, while the second term represents the change in thickness induced by the jump discontinuity. For isochoric plastic flow inside the shear band, $\boldsymbol{n} \cdot \llbracket \boldsymbol{\phi} \rrbracket = 0$, and there is no change in thickness induced by the jump component of deformation. With a dilatant plastic flow, $\boldsymbol{n} \cdot \llbracket \boldsymbol{\phi} \rrbracket > 0$, and the shear band thickness grows with plastic deformation.

2.2. Microscale constitutive formulation

The constitutive response of a damaged material is not necessarily related to the constitutive response of an intact continuum. This implies that the pre-localized constitutive model does not necessarily carry over to the post-localized regime. This statement has some physical justifications. For example, the constitutive response of an intact rock cannot be used to describe the constitutive behavior of the particulate material derived from this parent rock once this material has experienced strain localization. This idea is now pursued in the formulation of a finite strain constitutive model for the microscale field discussed in the following.

For the case of isotropy the hyperelastic constitutive equation takes the form [30]

$$\boldsymbol{\tau} = 2\frac{\partial \psi}{\partial \boldsymbol{b}^{\mathrm{e}}} \cdot \boldsymbol{b}^{\mathrm{e}} = 2\boldsymbol{b}^{\mathrm{e}} \cdot \frac{\partial \psi}{\partial \boldsymbol{b}^{\mathrm{e}}}, \tag{2.11}$$

where ψ is the free energy function and $\boldsymbol{b}^{\mathrm{e}}$ is the elastic left Cauchy–Green deformation tensor. Following the multiplicative decomposition $\boldsymbol{F} = \boldsymbol{F}^{\mathrm{e}} \cdot \boldsymbol{F}^{\mathrm{p}}$ proposed in [39], $\boldsymbol{b}^{\mathrm{e}}$ is obtained as

$$\boldsymbol{b}^{\mathrm{e}} = \boldsymbol{F}^{\mathrm{e}} \cdot \boldsymbol{F}^{\mathrm{e}t} = \boldsymbol{F} \cdot \boldsymbol{C}^{\mathrm{p}-1} \cdot \boldsymbol{F}^{t}, \tag{2.12}$$

where $\boldsymbol{C}^{\mathrm{p}} = \boldsymbol{F}^{\mathrm{p}t} \cdot \boldsymbol{F}^{\mathrm{p}}$ is the plastic right Cauchy–Green deformation tensor.

The rate version of the hyperelastic constitutive equation is obtained from the chain rule as

$$\dot{\boldsymbol{\tau}} = \tfrac{1}{2}\boldsymbol{\varphi} : \dot{\boldsymbol{b}}^{\mathrm{e}}, \tag{2.13}$$

where $\boldsymbol{\varphi}$ is a rank-four tangential stress-deformation tensor of the form given in [30], and $\dot{\boldsymbol{b}}^{\mathrm{e}}$ is given by

$$\dot{\boldsymbol{b}}^{\mathrm{e}} = (\boldsymbol{l} - \boldsymbol{l}^{\mathrm{p}}) \cdot \boldsymbol{b}^{\mathrm{e}} + \boldsymbol{b}^{\mathrm{e}} \cdot (\boldsymbol{l} - \boldsymbol{l}^{\mathrm{p}})^{t}. \tag{2.14}$$

Here we have defined (see [40])

$$\boldsymbol{l}^{\mathrm{p}} := \boldsymbol{F}^{\mathrm{e}} \cdot \boldsymbol{L}^{\mathrm{p}} \cdot \boldsymbol{F}^{\mathrm{e}-1}, \quad \boldsymbol{L}^{\mathrm{p}} := \dot{\boldsymbol{F}}^{\mathrm{p}} \cdot \boldsymbol{F}^{\mathrm{p}-1}. \tag{2.15}$$

Inserting into (2.13) yields

$$\dot{\boldsymbol{\tau}} = \boldsymbol{\alpha}^{\mathrm{e}} : (\boldsymbol{l} - \boldsymbol{l}^{\mathrm{p}}) \equiv \boldsymbol{\alpha}^{\mathrm{e}} : \boldsymbol{l}^{\mathrm{e}}, \tag{2.16}$$

where $\boldsymbol{l}^{\mathrm{e}} := \boldsymbol{l} - \boldsymbol{l}^{\mathrm{p}}$, and $\boldsymbol{\alpha}^{\mathrm{e}}$ is a spatial elastic tangent operator which takes the form (see [30])

$$\boldsymbol{\alpha}^{\mathrm{e}} = \mathbf{a}^{\mathrm{e}} + \boldsymbol{\tau} \ominus \mathbf{1}, \tag{2.17}$$

in which $(\boldsymbol{\tau} \ominus \mathbf{1})_{ijkl} = \tau_{il}\delta_{jk}$. The two-point spatial tensor $\mathbf{a}$ has components

$$\mathsf{a}_{ikjl} = F_{kA}F_{lB}\mathsf{A}_{iAjB}, \quad \mathsf{A}_{iAjB} = \frac{\partial P_{iA}}{\partial F_{jB}}, \tag{2.18}$$

where P_{iA} and F_{jB} are elements of the first Piola–Kirchhoff stress tensor $\boldsymbol{P}$ and the deformation gradient $\boldsymbol{F}$, respectively. The tensor $\boldsymbol{\varphi}$ operates in such a way that $\boldsymbol{\varphi} : (\boldsymbol{\psi} \cdot \boldsymbol{b}^{\mathrm{e}} + \boldsymbol{b}^{\mathrm{e}} \cdot \boldsymbol{\psi}^{t}) = 2\boldsymbol{\alpha}^{\mathrm{e}} : \boldsymbol{\psi}$ for any second-order tensor $\boldsymbol{\psi}$.

Next, let us consider a *bifurcated* yield function $\mathscr{G} = \mathscr{G}(\boldsymbol{\tau}, \tau_Y) = 0$ of the Kirchhoff stress tensor $\boldsymbol{\tau}$ characterizing yielding of the damaged material inside the band. Here, the elastic region inside the band is defined by the set

$$\boldsymbol{E}' = \{(\boldsymbol{\tau}, \tau_Y) \in S \times R^{1+} | \mathscr{G}(\boldsymbol{\tau}, \tau_Y) \leqslant 0\}, \tag{2.19}$$

where S is the space of symmetric second-order tensors. Once again, we note that $\mathscr{G}$ is generally not related to the pre-localized yield function $\mathscr{F}$ characterizing the yield function for the intact material. In addition,

we assume the following flow rules for the symmetric and skew-symmetric parts of the plastic component of the velocity gradient

$$\boldsymbol{d}^{\mathrm{p}} := \mathrm{sym}[\boldsymbol{l}^{\mathrm{p}}] = \lambda \boldsymbol{r}, \quad \boldsymbol{\omega}^{\mathrm{p}} := \mathrm{skew}[\boldsymbol{l}^{\mathrm{p}}] = \lambda \boldsymbol{r}', \quad \boldsymbol{l}^{\mathrm{p}} = \boldsymbol{d}^{\mathrm{p}} + \boldsymbol{\omega}^{\mathrm{p}}, \tag{2.20}$$

where $\lambda > 0$ is a plastic multiplier, and $\boldsymbol{r}$ and $\boldsymbol{r}'$ define the directions of the plastic rate of deformation and plastic spin tensors, respectively. In the absence of strain localization it is common to ignore the plastic spin [40]; however, in the presence of strain localization this is not the case since the slip tensor naturally contains a skew-symmetric part, as elaborated further in the following developments.

With the above flow rules, we can now write the rate constitutive equation inside the band as

$$\dot{\boldsymbol{\tau}} = \boldsymbol{\alpha}^{\mathrm{e}} : (\boldsymbol{l} - \boldsymbol{l}^{\mathrm{p}}) = \boldsymbol{\alpha}^{\mathrm{e}} : [\bar{\boldsymbol{l}} + (\overset{\nabla}{[\![\boldsymbol{\phi}]\!]} \otimes \boldsymbol{n})/h - \lambda(\boldsymbol{r} + \boldsymbol{r}')]. \tag{2.21}$$

Letting $\boldsymbol{g} = \partial \mathscr{G}/\partial \boldsymbol{\tau}$, the consistency condition inside the band now reads

$$\dot{\mathscr{G}} = \boldsymbol{g} : \dot{\boldsymbol{\tau}} - \lambda \mathscr{H} = 0, \tag{2.22}$$

where $\mathscr{H}$ is the *softening* modulus inside the band. Following standard lines [24–27,31,34,35], elastic unloading outside the band can be captured by assuming $\mathscr{H}$ to take the form

$$\mathscr{H} = \mathscr{H}_{\delta} h = \mathrm{O}(h), \tag{2.23}$$

where $\mathscr{H}_{\delta} < 0$. Equation (2.22) then leads to an expression for the plastic multiplier of the form

$$\lambda = \bar{\lambda} + \frac{1}{h}\lambda_{\delta}, \tag{2.24}$$

where

$$\bar{\lambda} = \frac{1}{\hat{\chi}} \boldsymbol{g} : \boldsymbol{\alpha}^{\mathrm{e}} : \bar{\boldsymbol{l}}, \quad \lambda_{\delta} = \frac{1}{\hat{\chi}} \boldsymbol{g} : \boldsymbol{\alpha}^{\mathrm{e}} : (\overset{\nabla}{[\![\phi]\!]} \otimes \boldsymbol{n}), \quad \hat{\chi} = \boldsymbol{g} : \boldsymbol{\alpha}^{\mathrm{e}} : (\boldsymbol{r} + \boldsymbol{r}') + \mathscr{H}_{\delta} h, \tag{2.25}$$

and where the hat symbol $(\hat{\cdot})$ is used to suggest that the post-bifurcation constitutive model is now invoked. In the unregularized formulation $\bar{\lambda}$ may be conveniently set to zero since $\lambda \to \lambda_{\delta}\delta_{\mathscr{S}}$ as $h \to 0$, where $\delta_{\mathscr{S}}$ is the Dirac delta function [24–26,31,34,35].

Inserting (2.25) into the constitutive equation (2.21) yields the following expression for the material Kirchhoff stress rate inside the band

$$\dot{\boldsymbol{\tau}}^{1} = \hat{\boldsymbol{\alpha}}^{\mathrm{ep}} : \left[\bar{\boldsymbol{l}} + \frac{1}{h}(\overset{\nabla}{[\![\boldsymbol{\phi}]\!]} \otimes \boldsymbol{n})\right], \tag{2.26}$$

where the superscript "1" implies "inside the band," and

$$\hat{\boldsymbol{\alpha}}^{\mathrm{ep}} = \boldsymbol{\alpha}^{\mathrm{e}} - \frac{1}{\hat{\chi}} \boldsymbol{\alpha}^{\mathrm{e}} : (\boldsymbol{r} + \boldsymbol{r}') \otimes \boldsymbol{g} : \boldsymbol{\alpha}^{\mathrm{e}} \tag{2.27}$$

is the elastoplastic tangential moduli tensor in the bifurcated state. As $h \to 0$, $\hat{\chi} \to \boldsymbol{g} : \boldsymbol{\alpha}^{\mathrm{e}} : (\boldsymbol{r} + \boldsymbol{r}')$, and $\hat{\boldsymbol{\alpha}}^{\mathrm{ep}}$ approaches the perfectly plastic tangent tensor.

2.3. General evolution condition for the shear band

The localization condition pertains to the onset of discontinuity, while the evolution condition pertains to the continued activation of a preexisting discontinuity. There is a conceptual difference between the two conditions, the most notable being that the localization condition is developed from a stability analysis requiring the solution of an eigenvalue problem, whereas the evolution condition is derived from a deformation analysis that specifies the character of an acceptable shear band.

For simplicity, attention is restricted to the usual quasi-static problem focusing on the evolution of a preexisting shear band. The weak form of the linear momentum balance reads

$$\int_{\mathscr{B}} (\mathrm{GRAD}\,\boldsymbol{\eta} : \boldsymbol{P} - \rho_0 \boldsymbol{\eta} \cdot \boldsymbol{G})\,\mathrm{d}V - \int_{\partial\mathscr{B}^t} \boldsymbol{\eta} \cdot \boldsymbol{t}\,\mathrm{d}A = 0, \tag{2.28}$$

where $\rho_0 \boldsymbol{G}$ is the reference body force vector, $\boldsymbol{t} = \boldsymbol{P} \cdot \boldsymbol{v}$ is the *nominal* traction vector on $\partial\mathscr{B}^t \subset \partial\mathscr{B}$, $\boldsymbol{v}$ is the unit vector on $\partial\mathscr{B}^t$, and $\boldsymbol{\eta}$ is the weighting function. In the presence of a shear band we can use integration by parts and Gauss theorem on the first term to obtain

$$\int_{\mathscr{B}\setminus\widetilde{\mathscr{S}}_0} \mathrm{GRAD}\,\boldsymbol{\eta} : \boldsymbol{P}\,\mathrm{d}V = -\int_{\mathscr{B}\setminus\widetilde{\mathscr{S}}_0} \boldsymbol{\eta} \cdot \mathrm{DIV}\,\boldsymbol{P}\,\mathrm{d}V + \int_{\widetilde{\mathscr{S}}_0} \boldsymbol{\eta} \cdot (\llbracket \boldsymbol{P} \cdot \boldsymbol{N} \rrbracket)\,\mathrm{d}A + \int_{\partial\mathscr{B}^t} \boldsymbol{\eta} \cdot (\boldsymbol{P} \cdot \boldsymbol{v})\,\mathrm{d}A, \tag{2.29}$$

where $\boldsymbol{N}$ is the unit normal vector to a preexisting shear band $\widetilde{\mathscr{S}}_0$, and $\llbracket \boldsymbol{P} \cdot \boldsymbol{N} \rrbracket$ is a possible jump in the nominal traction vector across $\widetilde{\mathscr{S}}_0$. Inserting into (2.28), a standard argument yields

$$\mathrm{DIV}\boldsymbol{P} + \rho_0 \boldsymbol{G} = \boldsymbol{0} \quad \text{in } \mathscr{B} \setminus \widetilde{\mathscr{S}}_0; \tag{2.30a}$$

$$\boldsymbol{P} \cdot \boldsymbol{v} = \boldsymbol{t} \quad \text{on } \partial\mathscr{B}^t, \tag{2.30b}$$

supplemented with the condition

$$\llbracket \boldsymbol{P} \cdot \boldsymbol{N} \rrbracket = \llbracket \boldsymbol{P} \rrbracket \cdot \boldsymbol{N} = \boldsymbol{0} \quad \text{on } \widetilde{\mathscr{S}}_0. \tag{2.31}$$

This suggests that the nominal traction vector $\boldsymbol{t}$, or, equivalently, its rate, $\dot{\boldsymbol{t}} = \llbracket \dot{\boldsymbol{P}} \rrbracket \cdot \boldsymbol{N}$, must remain continuous across the band.

From the chain rule, we obtain the time derivative of $\boldsymbol{P} = \boldsymbol{\tau} \cdot \boldsymbol{F}^{-t}$ as

$$\dot{\boldsymbol{P}} = \dot{\boldsymbol{\tau}} \cdot \boldsymbol{F}^{-t} - \boldsymbol{\tau} \cdot \boldsymbol{l}^t \cdot \boldsymbol{F}^{-t}. \tag{2.32}$$

Evaluating just outside $\widetilde{\mathscr{S}}_0$, where

$$\dot{\boldsymbol{\tau}}^0 = \boldsymbol{\alpha}^{\mathrm{e}} : \bar{\boldsymbol{l}}, \quad \boldsymbol{l} = \bar{\boldsymbol{l}}, \quad \boldsymbol{F} = \overline{\boldsymbol{F}}, \quad \dot{\boldsymbol{F}} = \dot{\overline{\boldsymbol{F}}}, \tag{2.33}$$

we get

$$\dot{\boldsymbol{P}}^0 = \overline{\mathbf{A}}^{\mathrm{e}} : \dot{\overline{\boldsymbol{F}}}, \tag{2.34}$$

where $\overline{\mathbf{A}}^{\mathrm{e}}$ is the first tangential elasticity tensor evaluated just outside the band, with components

$$\overline{\mathsf{A}}^{\mathrm{e}}_{iAjB} = \overline{F}^{-1}_{Ak} \overline{F}^{-1}_{Bl} \mathsf{a}^{\mathrm{e}}_{ikjl}, \quad \mathsf{a}^{\mathrm{e}}_{ikjl} = \alpha^{\mathrm{e}}_{ikjl} - \tau^0_{il}\delta_{jk}. \tag{2.35}$$

The overline on $\overline{\mathbf{A}}^{\mathrm{e}}$ denotes a pull-back induced by the operator $\overline{\boldsymbol{F}}^{-1}$.

Next let us evaluate (2.32) just inside $\widetilde{\mathscr{S}}_0$, but now using expressions for $\boldsymbol{F}^{-1}$, $\boldsymbol{l}$, and $\dot{\boldsymbol{\tau}}$ inside the band. After some mathematical manipulations, we get

$$\dot{\boldsymbol{P}}^1 = \widehat{\mathbf{A}}^{\mathrm{ep}} : \left[\dot{\overline{\boldsymbol{F}}} + \frac{1}{h_0} (\llbracket \dot{\boldsymbol{\phi}} \rrbracket \otimes \boldsymbol{N}) \right], \tag{2.36}$$

where $\widehat{\mathbf{A}}^{\mathrm{ep}}$ is the first tangential elastoplastic moduli tensor with components

$$\widehat{\mathsf{A}}^{\mathrm{ep}}_{iAjB} = F^{-1}_{Ak} F^{-1}_{Bl} \widehat{\mathsf{a}}^{\mathrm{ep}}_{ikjl}, \quad \widehat{\mathsf{a}}^{\mathrm{ep}}_{ikjl} = \widehat{\alpha}^{\mathrm{ep}}_{ikjl} - \tau^1_{il}\delta_{jk}. \tag{2.37}$$

Note that the pull-back inside the band is now induced by the full operator $\boldsymbol{F}^{-1}$. The evolution condition can now be written as

$$(\dot{\boldsymbol{P}}^1 - \dot{\boldsymbol{P}}^0) \cdot \boldsymbol{N} = \boldsymbol{0} \quad \text{on } \widetilde{\mathscr{S}}_0, \quad \forall t > t_{\mathrm{b}}, \tag{2.38}$$

where $t_{\rm b}$ is the bifurcation point. The latter expression is equivalent to

$$\left[\left(\widehat{\mathbf{A}}^{\rm ep}-\bar{\mathbf{A}}^{\rm e}\right):\dot{\bar{\boldsymbol{F}}}\right]\cdot\boldsymbol{N}+\frac{1}{h_0}\widehat{\boldsymbol{A}}\cdot[\![\dot{\boldsymbol{\phi}}]\!]=\mathbf{0},\qquad \widehat{A}_{ij}=N_A\widehat{\mathsf{A}}^{\rm ep}_{iAjB}N_B, \tag{2.39}$$

where $\widehat{\boldsymbol{A}}$ is the Lagrangian elastoplastic acoustic tensor. This is the general evolution condition that must be satisfied by the shear band.

2.4. Specialization to strong discontinuity

The limiting condition of strong discontinuity is of special interest since it provides a convenient finite element implementation within the framework of embedded discontinuities. The evolution condition is derived from (2.39) in the limit of a vanishing shear band thickness. As $h_0\to 0$ the first term remains a regular function while the second term increases without bounds. In order for the jump in the traction rate to remain bounded, we must have

$$\widehat{\boldsymbol{A}}\cdot[\![\dot{\boldsymbol{\phi}}]\!]=\mathbf{0},\quad \forall t>t_b. \tag{2.40}$$

This is the Lagrangian evolution condition in the strong discontinuity limit.

A spatial counterpart of the evolution condition may be derived by rewriting the jump condition (2.38) in the form (after skipping some details)

$$\left[\left(\frac{h_0}{h}\widehat{\mathbf{a}}^{\rm ep}-\frac{h_0+\boldsymbol{N}\cdot\boldsymbol{\Phi}}{h}\mathbf{a}^{\rm e}\right):\bar{\boldsymbol{l}}\right]\cdot\boldsymbol{n}+\frac{h_0}{h^2}\widehat{\boldsymbol{a}}\cdot[\![\overset{\triangledown}{\phi}]\!]=\mathbf{0}, \tag{2.41}$$

where

$$\widehat{a}_{ij}=n_k\widehat{\mathsf{a}}^{\rm ep}_{ikjl}n_l. \tag{2.42}$$

Note that

$$\frac{h_0}{h}=\boldsymbol{N}\cdot\boldsymbol{F}^{-1}\cdot\boldsymbol{n},\quad \frac{h_0+\boldsymbol{N}\cdot\boldsymbol{\Phi}}{h}=\boldsymbol{N}\cdot\bar{\boldsymbol{F}}^{-1}\cdot\boldsymbol{n}, \tag{2.43}$$

which are both regular functions for non-collapsing shear band, see [41]. Multiplying (2.41) by h/h_0 gives

$$\left[\left(\widehat{\mathbf{a}}^{\rm ep}-\frac{h_0+\boldsymbol{N}\cdot\boldsymbol{\Phi}}{h_0}\mathbf{a}^{\rm e}\right):\bar{\boldsymbol{l}}\right]\cdot\boldsymbol{n}+\frac{1}{h}\widehat{\boldsymbol{a}}\cdot[\![\overset{\triangledown}{\phi}]\!]=\mathbf{0}. \tag{2.44}$$

As $h\to 0$ the first term remains a regular function while the second term increases without bounds, unless we set

$$\widehat{\boldsymbol{a}}\cdot[\![\overset{\triangledown}{\phi}]\!]=\mathbf{0},\quad \forall t>t_b. \tag{2.45}$$

This is the Eulerian evolution condition in the strong discontinuity limit. Note that the equivalence of (2.40) and (2.45) can only be established in the strong discontinuity limit.

Let us expand (2.45) using indicial notation,

$$n_k\widehat{\alpha}^{\rm ep}_{ikjl}n_l[\![\overset{\triangledown}{\phi}_j]\!]-\tau_{il}n_ln_k[\![\overset{\triangledown}{\phi}_k]\!]=0,\quad \forall t>t_{\rm b}. \tag{2.46}$$

The first term is identically zero if we define the slip tensor as

$$[\![\overset{\triangledown}{\boldsymbol{\phi}}]\!]\otimes\boldsymbol{n}=\lambda_\delta(\boldsymbol{r}+\boldsymbol{r}'),\quad \forall t>t_{\rm b}, \tag{2.47}$$

where $\boldsymbol{r}$ and $\boldsymbol{r}'$ are the directions of the plastic rate of deformation tensor $\boldsymbol{d}^{\rm p}$ and plastic spin tensor $\boldsymbol{\omega}^{\rm p}$ "inside the band", respectively. That this is the case may be demonstrated from

$$\widehat{\boldsymbol{\alpha}}^{\mathrm{ep}} : (\overset{\nabla}{[\![\boldsymbol{\phi}]\!]} \otimes \boldsymbol{n}) = \widehat{\boldsymbol{\alpha}}^{\mathrm{ep}} : \lambda_\delta(\boldsymbol{r}+\boldsymbol{r}') = \left[\boldsymbol{\alpha}^{\mathrm{e}} - \frac{\boldsymbol{\alpha}^{\mathrm{e}} : (\boldsymbol{r}+\boldsymbol{r}') \otimes \boldsymbol{g} : \boldsymbol{\alpha}^{\mathrm{e}}}{\boldsymbol{g} : \boldsymbol{\alpha}^{\mathrm{e}} : (\boldsymbol{r}+\boldsymbol{r}')}\right] : \lambda_\delta(\boldsymbol{r}+\boldsymbol{r}') \equiv \boldsymbol{0}, \tag{2.48}$$

since any tensor $\boldsymbol{\psi} \propto (\boldsymbol{r}+\boldsymbol{r}')$ lies in the null space of $\widehat{\boldsymbol{\alpha}}^{\mathrm{ep}}$ (by construction). The choice of λ_δ as the scaling parameter is imposed by the requirement that the Kirchhoff stress rate given by (2.21) remains regular even if h approaches zero. This implies that the slip tensor $(\overset{\nabla}{[\![\boldsymbol{\phi}]\!]} \otimes \boldsymbol{n})$ is fully plastic, a similar conclusion developed for the infinitesimal case [24].

It remains to satisfy the condition that the second term in (2.46) must vanish identically in the post-bifurcation regime. Since $\tau_{il} n_l \neq 0$, we must have

$$n_k \overset{\nabla}{[\![\phi_k]\!]} = \boldsymbol{n} \cdot \overset{\nabla}{[\![\boldsymbol{\phi}]\!]} = \lambda_\delta r_{kk} = \lambda_\delta \mathrm{tr}(\boldsymbol{r}) = 0, \quad \forall t > t_{\mathrm{b}}, \tag{2.49}$$

which means that the plastic flow "inside the band" must be isochoric. This can easily be satisfied by requiring that the objective velocity jump vector $\overset{\nabla}{[\![\boldsymbol{\phi}]\!]}$ be perpendicular to the current normal vector $\boldsymbol{n}$, i.e., $\overset{\nabla}{[\![\boldsymbol{\phi}]\!]}$ must be tangent to the band. Note that the plastic directions $\boldsymbol{r}$ and $\boldsymbol{r}'$ need not be known, but the above kinematical constraints must be considered when embedding discontinuities into the finite elements (with the AES method this constraint affects the form of the weighting function for the enhancement equation). Since the objective velocity jump vector $\overset{\nabla}{[\![\boldsymbol{\phi}]\!]}$ remains tangent to the band, the cumulative displacement jump vector $[\![\boldsymbol{\phi}]\!]$ also remains tangent to the band.

From a physical standpoint the kinematical restriction to $\overset{\nabla}{[\![\boldsymbol{\phi}]\!]}$ implies that no relative normal displacement may occur between the opposite surfaces of the band if a strong discontinuity is to remain a strong discontinuity. While this may seem obvious, this requirement is in fact not present in the infinitesimal formulation since the stress term that brings about this kinematical constraint does not appear in the small-strain constitutive formulation [24,25]. These features are now incorporated into the finite element model discussed in the next section.

3. Formulation of finite element multiscale model

For simplicity we restrict the following presentation to quasi-static loading. The finite element approximations are based on a standard weak equation (2.28), which is rewritten herein for a typical localized finite element $\mathscr{B}^{\mathrm{e}}$ as follows

$$\int_{\mathscr{B}^{\mathrm{e}}} \mathrm{GRAD}\,\boldsymbol{\eta} : \boldsymbol{P}\,\mathrm{d}V = \int_{\mathscr{B}^{\mathrm{e}}} \rho_0 \boldsymbol{\eta} \cdot \boldsymbol{G}\,\mathrm{d}V + \int_{\partial\mathscr{B}^{\mathrm{e}}} \boldsymbol{\eta} \cdot \boldsymbol{t}\,\mathrm{d}A. \tag{3.1}$$

The left-hand side of the above equation is the internal virtual work, which can be written in spatial form as

$$W^{\mathrm{e}}_{\mathrm{INT}} = \int_{\mathscr{B}^{\mathrm{e}}} \mathrm{GRAD}\,\boldsymbol{\eta} : \boldsymbol{P}\,\mathrm{d}V = \int_{\mathscr{B}^{\mathrm{e}}} \mathrm{GRAD}\,\boldsymbol{\eta} : \boldsymbol{\tau} \cdot \overline{\boldsymbol{F}}^{-t}\,\mathrm{d}V = \int_{\mathscr{B}^{\mathrm{e}}} \bar{\mathrm{g}}\mathrm{rad}\,\boldsymbol{\eta} : \boldsymbol{\tau}\,\mathrm{d}V, \tag{3.2}$$

where $\bar{\mathrm{g}}\mathrm{rad}\,\boldsymbol{\eta} = \partial\boldsymbol{\eta}/\partial\bar{\boldsymbol{x}}$. We emphasize that $\boldsymbol{P}$ is the first Piola–Kirchhoff stress tensor evaluated just outside the band, which is related to the symmetric Kirchhoff stress tensor $\boldsymbol{\tau}$ outside the band by the deformation gradient $\overline{\boldsymbol{F}}$ of the *continuous* part of motion, see (2.3). Consequently, the spatial form of $W^{\mathrm{e}}_{\mathrm{INT}}$ now utilizes a local gradient of the weighting function $\boldsymbol{\eta}$ with respect to the coordinates $\bar{\boldsymbol{x}}$ of the continuous configuration. Our goal in this section is to formulate a constitutive expression for $\boldsymbol{\tau}$ in terms of the deformation gradient of the *conforming* part of motion, leading to a Petrov–Galerkin formulation.

Also, from previous developments, we recall that continued activation of a strong discontinuity represented by the surface $\mathscr{S}^{\mathrm{e}}$ intersecting $\mathscr{B}^{\mathrm{e}}$ is contingent upon the satisfaction of the local evolution condition

$$[\![\dot{\boldsymbol{P}}]\!]\cdot\boldsymbol{N}=\boldsymbol{0}\quad\Longleftrightarrow\quad\widehat{\boldsymbol{A}}\cdot[\![\overset{\nabla}{\boldsymbol{\phi}}]\!]=\boldsymbol{0},\quad\forall t>t_{\mathrm{b}}. \tag{3.3}$$

As demonstrated in Section 2, this requires that $([\![\overset{\nabla}{\boldsymbol{\phi}}]\!]\otimes\boldsymbol{n})$ be fully plastic and that the objective jump velocity vector $[\![\overset{\nabla}{\boldsymbol{\phi}}]\!]$ be tangent to $\phi(\mathscr{S}^{\mathrm{e}})$.

3.1. Discrete kinematics of localized element

Consider a typical triangulation shown in Fig. 1 and let the surface of discontinuity be denoted by $\mathscr{S}$. The compact support is $\mathscr{B}^h=\mathscr{B}^h_-\cup\mathscr{B}^h_+$, denoted by the shaded region in Fig. 1, and consists of all CST elements traced by the shear band. A typical localized element $\mathscr{B}^{\mathrm{e}}\in\mathscr{B}^h$ is shown in Fig. 2. A discontinuous displacement field $\boldsymbol{u}$ inside this element is represented by the equation

$$\boldsymbol{u}(\boldsymbol{X})=\bar{\boldsymbol{u}}(\boldsymbol{X})+[\![\boldsymbol{u}]\!]H_{\mathscr{S}}(\boldsymbol{X}),\quad H_{\mathscr{S}}(\boldsymbol{X})=\begin{cases}1 & \text{if } \boldsymbol{X}\in\mathscr{B}^{\mathrm{e}}_+,\\ 0 & \text{if } \boldsymbol{X}\in\mathscr{B}^{\mathrm{e}}_-,\end{cases} \tag{3.4}$$

where $\bar{\boldsymbol{u}}$ is the continuous part of $\boldsymbol{u}$, and $[\![\boldsymbol{u}]\!]$ is the jump discontinuity on $\mathscr{S}^{\mathrm{e}}$. Here, we assume that $[\![\boldsymbol{u}]\!]$ is spatially constant in $\mathscr{B}^{\mathrm{e}}$ but may be discontinuous across the element boundaries. More precisely, we have

$$[\![\boldsymbol{u}]\!]=\zeta\boldsymbol{m}, \tag{3.5}$$

where ζ is the magnitude of the jump, and $\boldsymbol{m}$ is the unit vector in the direction of the jump. Note that $[\![\boldsymbol{u}]\!]$ is always co-rotational with the surface of discontinuity.

The same discontinuous displacement field may be written in a reparameterized form

$$\boldsymbol{u}(\boldsymbol{X})=\tilde{\boldsymbol{u}}(\boldsymbol{X})+[\![\boldsymbol{u}]\!]M_{\mathscr{S}}(\boldsymbol{X}), \tag{3.6}$$

where the jump of $M_{\mathscr{S}}$ across $\mathscr{S}^{\mathrm{e}}$ is $[\![M_{\mathscr{S}}]\!]=1$, with $M_{\mathscr{S}}=0$ on the surface $\mathscr{S}^h_\pm$ of the support $\mathscr{B}^h$. A comparison of (3.6) with (3.4) suggests that $\tilde{\boldsymbol{u}}=\bar{\boldsymbol{u}}$ in $\mathscr{B}_-\setminus\mathscr{B}^h_-$, and $\tilde{\boldsymbol{u}}=\bar{\boldsymbol{u}}+[\![\boldsymbol{u}]\!]$ in $\mathscr{B}_+\setminus\mathscr{B}^h_+$, and so $\tilde{\boldsymbol{u}}$ simply describes the *conforming* total displacement field, i.e., the displacement field that conforms with the element nodal displacements and the standard element shape functions, see Fig. 2. Conforming fields are also referred to as the *coarse-scale field* by some authors [19–22]. The jump function $M_{\mathscr{S}}$ may be taken as

$$M_{\mathscr{S}}(\boldsymbol{X})=H_{\mathscr{S}}(\boldsymbol{X})-f^h(\boldsymbol{X}), \tag{3.7}$$

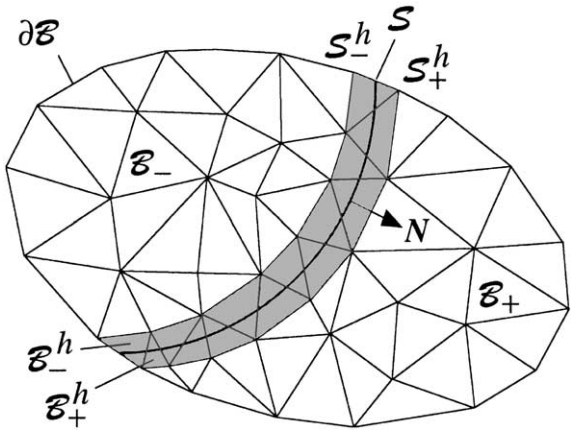

Fig. 1. Definition of surface discontinuity.

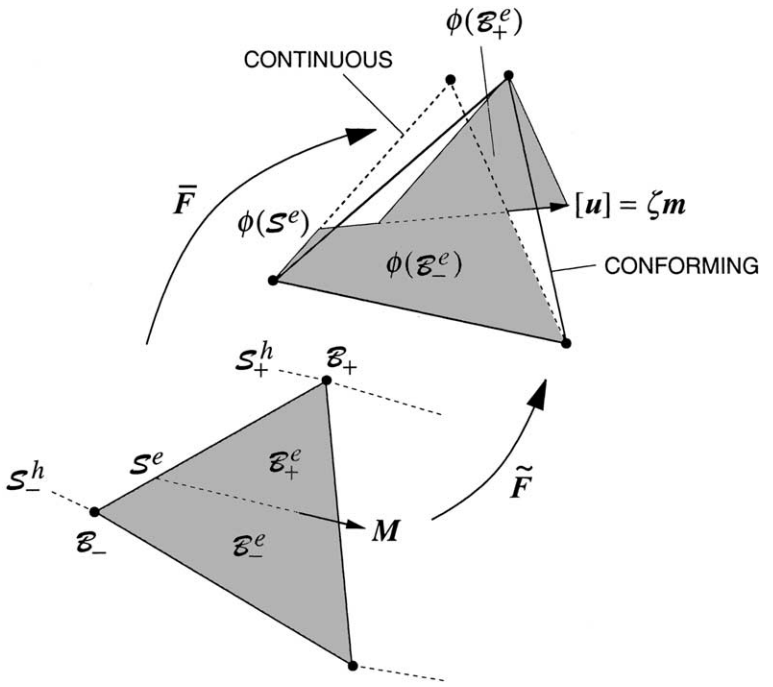

Fig. 2. Conforming and continuous deformations in a localized CST element. Note: shaded region represents the total configuration $\boldsymbol{\phi}$.

where f^h is any arbitrary smooth ramp function that satisfies the requirement that $f^h = 0$ in $\mathscr{B}_- \setminus \mathscr{B}_-^h$, and $f^h = 1$ in $\mathscr{B}_+ \setminus \mathscr{B}_+^h$. Note that f^h is not meant to approximate the Heaviside function $H_{\mathscr{S}}$ since any acceptable form for this function can always be combined with $M_{\mathscr{S}}$ to obtain the exact Heaviside function. The term $[\![\boldsymbol{u}]\!]M_{\mathscr{S}}(\boldsymbol{X})$ is sometimes referred to as the *fine-scale field*, so that (3.6) may be interpreted as an additive decomposition of the total displacement field into coarse-scale and fine-scale components [21,22]. With these parameterizations, the spatial coordinates of the continuous part of motion can be written as

$$\bar{\boldsymbol{x}} = \boldsymbol{X} + \bar{\boldsymbol{u}} = \boldsymbol{X} + \tilde{\boldsymbol{u}}(\boldsymbol{X}) - [\![\boldsymbol{u}]\!] f^h(\boldsymbol{X}), \quad \boldsymbol{X} \in \mathscr{B}^{\mathrm{e}}. \tag{3.8}$$

The continuous deformation map for the same CST element is also shown pictorially in Fig. 2.

Let us denote the coordinates of the conforming part of motion in $\mathscr{B}^{\mathrm{e}}$ at time instants t_n and $t > t_n$, respectively, by

$$\tilde{\boldsymbol{x}}_n = \boldsymbol{X} + \tilde{\boldsymbol{u}}_n, \quad \tilde{\boldsymbol{x}} = \boldsymbol{X} + \tilde{\boldsymbol{u}}. \tag{3.9}$$

The coordinates of the corresponding continuous part of motion are

$$\bar{\boldsymbol{x}}_n = \tilde{\boldsymbol{x}}_n - \zeta_n \boldsymbol{m}_n f^h, \quad \bar{\boldsymbol{x}} = \tilde{\boldsymbol{x}} - \zeta \boldsymbol{m} f^h. \tag{3.10}$$

Let us also define the following deformation gradients:

$$\bar{\boldsymbol{F}}_n = \frac{\partial \bar{\boldsymbol{x}}_n}{\partial \boldsymbol{X}}, \quad \tilde{\boldsymbol{F}}_n = \frac{\partial \tilde{\boldsymbol{x}}_n}{\partial \boldsymbol{X}}, \quad \bar{\boldsymbol{F}} = \frac{\partial \bar{\boldsymbol{x}}}{\partial \boldsymbol{X}}, \quad \tilde{\boldsymbol{F}} = \frac{\partial \tilde{\boldsymbol{x}}}{\partial \boldsymbol{X}}. \tag{3.11}$$

From these, and from the assumed spatial constancy of the jump function $[\![\boldsymbol{u}]\!]$, we easily establish the relationships

$$\bar{\boldsymbol{F}}_n = \tilde{\boldsymbol{F}}_n - \zeta_n \boldsymbol{m}_n \otimes \frac{\partial f^h}{\partial \boldsymbol{X}}, \quad \bar{\boldsymbol{F}} = \tilde{\boldsymbol{F}} - \zeta \boldsymbol{m} \otimes \frac{\partial f^h}{\partial \boldsymbol{X}}. \tag{3.12}$$

Let us also define a relative deformation gradient that maps the continuous part of the motion function $\bar{\boldsymbol{x}}$ with the configuration $\bar{\boldsymbol{x}}_n$, herein denoted by

$$\bar{\boldsymbol{f}} = \frac{\partial \bar{\boldsymbol{x}}}{\partial \bar{\boldsymbol{x}}_n} = \overline{\boldsymbol{F}} \cdot \overline{\boldsymbol{F}}_n^{-1}. \tag{3.13}$$

As demonstrated later in this section, the relative deformation gradient $\bar{\boldsymbol{f}}$ plays a key role in describing the discrete evolution of the stresses in the post-localized regime.

The inverse of $\overline{\boldsymbol{F}}_n$ can be determined explicitly with the aid of the Sherman–Morrison formula as

$$\overline{\boldsymbol{F}}_n^{-1} = \widetilde{\boldsymbol{F}}_n^{-1} + \frac{\zeta_n}{1-\zeta_n\beta_n} \widetilde{\boldsymbol{M}}_n \otimes \frac{\partial f^h}{\partial \widetilde{\boldsymbol{x}}_n}, \tag{3.14}$$

where

$$\widetilde{\boldsymbol{M}}_n = \widetilde{\boldsymbol{F}}_n^{-1} \cdot \boldsymbol{m}_n, \quad \beta_n = \widetilde{\boldsymbol{M}}_n \cdot \frac{\partial f^h}{\partial \boldsymbol{X}} = \boldsymbol{m}_n \cdot \frac{\partial f^h}{\partial \widetilde{\boldsymbol{x}}_n}. \tag{3.15}$$

Now, let us define the relative deformation gradient of the conforming part of motion

$$\widetilde{\boldsymbol{f}} = \frac{\partial \widetilde{\boldsymbol{x}}}{\partial \widetilde{\boldsymbol{x}}_n} = \widetilde{\boldsymbol{F}} \cdot \widetilde{\boldsymbol{F}}_n^{-1}, \tag{3.16}$$

which maps the conforming part of the motion function $\widetilde{\boldsymbol{x}}$ with the configuration $\widetilde{\boldsymbol{x}}_n$. Using (3.13) and the definitions for the deformation gradients $\overline{\boldsymbol{F}}$ and $\overline{\boldsymbol{F}}_n$, the relationship between the relative deformation gradients $\bar{\boldsymbol{f}}$ and $\widetilde{\boldsymbol{f}}$ can easily be established as

$$\bar{\boldsymbol{f}} = \widetilde{\boldsymbol{f}} + \overset{\nabla}{\boldsymbol{m}} \otimes \frac{\partial f^h}{\partial \widetilde{\boldsymbol{x}}_n}, \tag{3.17}$$

where

$$\overset{\nabla}{\boldsymbol{m}} = \frac{\zeta_n}{1-\zeta_n\beta_n} \widetilde{\boldsymbol{f}} \cdot \boldsymbol{m}_n - \frac{\zeta}{1-\zeta_n\beta_n} \boldsymbol{m}. \tag{3.18}$$

For future use let us also derive an expression for the inverse of the relative deformation gradient $\bar{\boldsymbol{f}}$,

$$\bar{\boldsymbol{f}}^{-1} = \frac{\partial \bar{\boldsymbol{x}}_n}{\partial \bar{\boldsymbol{x}}} = \overline{\boldsymbol{F}}_n \cdot \overline{\boldsymbol{F}}^{-1}. \tag{3.19}$$

Using the Sherman–Morrison formula once again, we get the inverse of $\overline{\boldsymbol{F}}$ as

$$\overline{\boldsymbol{F}}^{-1} = \widetilde{\boldsymbol{F}}^{-1} + \frac{\zeta}{1-\zeta\beta} \widetilde{\boldsymbol{M}} \otimes \frac{\partial f^h}{\partial \widetilde{\boldsymbol{x}}}, \tag{3.20}$$

where

$$\widetilde{\boldsymbol{M}} = \widetilde{\boldsymbol{F}}^{-1} \cdot \boldsymbol{m}, \quad \beta = \widetilde{\boldsymbol{M}} \cdot \frac{\partial f^h}{\partial \boldsymbol{X}} = \boldsymbol{m} \cdot \frac{\partial f^h}{\partial \widetilde{\boldsymbol{x}}}. \tag{3.21}$$

Thus, we have

$$\bar{\boldsymbol{f}}^{-1} = \widetilde{\boldsymbol{f}}^{-1} + \overset{\nabla}{\boldsymbol{m}}_n \otimes \frac{\partial f^h}{\partial \widetilde{\boldsymbol{x}}}, \tag{3.22}$$

where

$$\overset{\nabla}{\boldsymbol{m}}_n = \frac{\zeta}{1-\zeta\beta} \widetilde{\boldsymbol{f}}^{-1} \cdot \boldsymbol{m} - \frac{\zeta_n}{1-\zeta\beta} \boldsymbol{m}_n. \tag{3.23}$$

Note that $\bar{\boldsymbol{f}}$ coincides with $\widetilde{\boldsymbol{f}}$ when $\zeta = \zeta_n = 0$, i.e., when there is no jump discontinuity.

3.2. General stress point integration algorithm

Consider the case of a strong discontinuity in a continuum deforming at finite strain and assume that elastic unloading persists outside the band. In this case the Kirchhoff stress rate takes the form

$$\dot{\boldsymbol{\tau}}^0 = \boldsymbol{\alpha}^{\mathrm{e}} : \bar{\boldsymbol{l}}. \tag{3.24}$$

If the band remains active, then yielding on the band is governed by the consistency condition

$$\dot{\mathscr{G}} = \boldsymbol{g} : \dot{\boldsymbol{\tau}} - \widetilde{\mathscr{H}}_{\delta}\dot{\zeta} = 0, \tag{3.25}$$

where $\mathscr{G}$ is the post-localized yield function, $\boldsymbol{g} = \partial\mathscr{G}/\partial\boldsymbol{\tau}$, $\dot{\zeta} > 0$ is the magnitude of the slip rate, and $\widetilde{\mathscr{H}}_{\delta}$ is a plastic modulus which relates the rate of softening of the yield function with the slip rate (see [24,25]). The notion of a dual response of a macroscopic point traced by a strong discontinuity as discussed in [25] suggests that the stress rate just outside the band may be used in the above consistency condition.

Consider a shear band to emerge at time $t = t_{\mathrm{b}}$ where the current value of the elastic left Cauchy–Green deformation tensor is given by

$$\boldsymbol{b}^{\mathrm{e}}_{\mathrm{b}} = \boldsymbol{F}^{\mathrm{e}}_{\mathrm{b}} \cdot \boldsymbol{F}^{\mathrm{e}t}_{\mathrm{b}}, \quad \boldsymbol{F}^{\mathrm{e}}_{\mathrm{b}} = \frac{\partial \boldsymbol{x}_{\mathrm{b}}}{\partial \boldsymbol{x}^{\mathrm{u}}_{\mathrm{b}}}. \tag{3.26}$$

Here, $\boldsymbol{x}^{\mathrm{u}}_{\mathrm{b}}$ defines an unloaded configuration of the point just outside the band at the moment of bifurcation. Note that at the point of bifurcation the deformations are still conforming, and so the notion of an unloaded configuration still applies. Assuming plastic softening "inside the band", then elastic unloading persists outside the band, and the unloaded configuration $\boldsymbol{x}^{\mathrm{u}}_{\mathrm{b}}$ outside the band remains fixed at post-bifurcation. Thus, for any time $t > t_n > t_{\mathrm{b}}$, where t_n is any post-bifurcation time instant at which the configuration $\phi_n(\mathscr{B}^{\mathrm{e}})$ has been fully defined, we have

$$\boldsymbol{b}^{\mathrm{e}}(t > t_n) = \bar{\boldsymbol{f}} \cdot \boldsymbol{b}^{\mathrm{e}}_n \cdot \bar{\boldsymbol{f}}^t, \quad \boldsymbol{b}^{\mathrm{e}}_n = \bar{\boldsymbol{f}}_n \cdot \boldsymbol{b}^{\mathrm{e}}_b \cdot \bar{\boldsymbol{f}}^t_n, \quad \boldsymbol{X} \in \mathscr{B}^{\mathrm{e}}, \tag{3.27}$$

where $\bar{\boldsymbol{f}} = \partial\bar{\boldsymbol{x}}/\partial\bar{\boldsymbol{x}}_n$ and $\bar{\boldsymbol{f}}_n = \partial\bar{\boldsymbol{x}}_n/\partial\boldsymbol{x}_{\mathrm{b}}$ are the relative deformation gradients of the continuous part of motion introduced previously. A simple check demonstrates the validity of the latter equation: differentiating it with respect to time and recognizing that $\boldsymbol{b}^{\mathrm{e}}_n$ is fixed gives

$$\dot{\boldsymbol{b}}^{\mathrm{e}} = \bar{\boldsymbol{l}} \cdot \boldsymbol{b}^{\mathrm{e}} + \boldsymbol{b}^{\mathrm{e}} \cdot \bar{\boldsymbol{l}}^t, \quad \bar{\boldsymbol{l}} = \dot{\bar{\boldsymbol{f}}} \cdot \bar{\boldsymbol{f}}^{-1} = \frac{\partial \bar{\boldsymbol{v}}}{\partial \bar{\boldsymbol{x}}}. \tag{3.28}$$

On substitution of this equation into (2.13), we recover (3.24).

Let us now perform a stress-point integration for a localized element, borrowing some ideas from computational plasticity of continuum mechanics. The procedure consists of, first, calculating a trial elastic stress predictor $\boldsymbol{\tau}^{\mathrm{tr}}$ by freezing plastic slip on the band, checking for yielding on the band, and, finally, introducing a positive plastic slip parameter if yielding is detected on the band. Care must be taken in performing each of these steps in the geometrically nonlinear regime as the displacement jumps need to be transformed objectively.

A push-forward transformation on the vector $\boldsymbol{m}_n$ using the relative deformation gradient of the continuous part of motion gives

$$\boldsymbol{m} = \bar{\boldsymbol{f}} \cdot \boldsymbol{m}_n / \|\bar{\boldsymbol{f}} \cdot \boldsymbol{m}_n\|. \tag{3.29}$$

That the push forward of the tangent vector $\boldsymbol{m}$ is induced by $\bar{\boldsymbol{f}}$ is due to the fact that any point on the tangent space $\mathscr{S}$ lies in the domain of the continuous deformation map. Now, let us combine (3.29) with (3.17) and (3.18) to get

$$\bar{\boldsymbol{f}} \cdot \boldsymbol{m}_n = \|\bar{\boldsymbol{f}} \cdot \boldsymbol{m}_n\| \boldsymbol{m} = \frac{1}{1-\zeta_n \beta_n} \widetilde{\boldsymbol{f}} \cdot \boldsymbol{m}_n - \frac{\zeta \beta_n}{1-\zeta_n \beta_n} \boldsymbol{m}. \tag{3.30}$$

This implies that $\widetilde{\boldsymbol{f}} \cdot \boldsymbol{m}_n \propto \boldsymbol{m}$, and so

$$\boldsymbol{m} = \widetilde{\boldsymbol{f}} \cdot \boldsymbol{m}_n / \|\widetilde{\boldsymbol{f}} \cdot \boldsymbol{m}_n\| = \widetilde{\boldsymbol{F}} \cdot \boldsymbol{M} / \|\widetilde{\boldsymbol{F}} \cdot \boldsymbol{M}\|, \tag{3.31}$$

where $\boldsymbol{M}$ is the fixed unit tangent vector to $\mathscr{S}_0$ in the undeformed configuration. Hence, the transformation of $\boldsymbol{m}_n$ (or $\boldsymbol{M}$) may also be defined by the conforming motion. Since standard finite element formulations rely on conforming motions, the latter push-forward transformation using the operator $\widetilde{\boldsymbol{f}}$ (or $\widetilde{\boldsymbol{F}}$) offers a more direct approach of tracking the evolution of the tangent vector.

Let us next define the evolution of the slip magnitude from the equation

$$\zeta = \zeta_n + \Delta\zeta. \tag{3.32}$$

This, together with the discrete evolution equations (3.17) and (3.18), allows the evaluation of the elastic left Cauchy–Green deformation tensor from the standard expression

$$\boldsymbol{b}^{\mathrm{e}} = \bar{\boldsymbol{f}} \cdot \boldsymbol{b}^{\mathrm{e}}_n \cdot \bar{\boldsymbol{f}}^t. \tag{3.33}$$

A spectral decomposition of this tensor yields

$$\boldsymbol{b}^{\mathrm{e}} = \sum_{A=1}^{3} \lambda_A^2 \boldsymbol{n}^{(A)} \otimes \boldsymbol{n}^{(A)}, \tag{3.34}$$

where λ_A^2 are squares of the principal elastic stretches and $\boldsymbol{n}^{(A)}$ are the principal directions. Writing the stored energy function U in terms of the principal elastic logarithmic stretches $\varepsilon^{\mathrm{e}}_A = \ln(\lambda_A)$, the Kirchhoff stress tensor is then obtained from

$$\boldsymbol{\tau} = \sum_{A=1}^{3} \beta_A \boldsymbol{n}^{(A)} \otimes \boldsymbol{n}^{(A)}, \quad \beta_A = \frac{\partial U}{\partial \varepsilon_A}, \tag{3.35}$$

where β_A are the Kirchhoff principal stresses. In this development, we have assumed that isotropy persists outside the band so that the principal directions of $\boldsymbol{b}^{\mathrm{e}}$ and $\boldsymbol{\tau}$ remain coincident.

The elastic stress predictor phase consists of setting $\Delta\zeta = 0$ and checking the sign of the post-bifurcation scalar yield function $\mathscr{G}(\boldsymbol{\tau}^{\mathrm{tr}}, \tau_{y,n})$. Here, $\boldsymbol{\tau}^{\mathrm{tr}}$ is the trial elastic Kirchhoff stress tensor evaluated by freezing plastic slip ($\Delta\zeta = 0$), and $\tau_{y,n}$ is the yield strength on the band calculated from the previous converged load step. A negative sign of the trial $\mathscr{G}$ implies unloading on the band (dormant shear band), while a positive sign implies plastic yielding on the band (active shear band). For active yielding on the band a plastic corrector is invoked by introducing an incremental plastic multiplier $\Delta\zeta > 0$. The value of this parameter can be determined iteratively from the discrete consistency condition

$$(\mathscr{G}_{n+1} - \mathscr{G}_n)_{\mathscr{A}} - \widetilde{\mathscr{H}}_{\delta} \Delta\zeta = 0, \tag{3.36}$$

where $(\mathscr{G}_{n+1} - \mathscr{G}_n)_{\mathscr{A}}$ is the incremental change in the value of the yield function $\mathscr{G}$ due to changes in the stresses on the band, with the plastic state variable $\mathscr{A}$ of the yield function $\mathscr{G}$ held fixed, see [24]. The elastic predictor–plastic corrector algorithm just described is represented pictorially in Fig. 3.

Putting (3.36) in residual form, we have

$$r(\Delta\zeta) = (\mathscr{G}_{n+1} - \mathscr{G}_n)_{\mathscr{A}} - \widetilde{\mathscr{H}}_{\delta} \Delta\zeta. \tag{3.37}$$

The problem is to determine the value of $\Delta\zeta$ satisfying (3.35) that gives $r(\Delta\zeta) = 0$. Using Newton's method, we evaluate the consistent tangent operator as

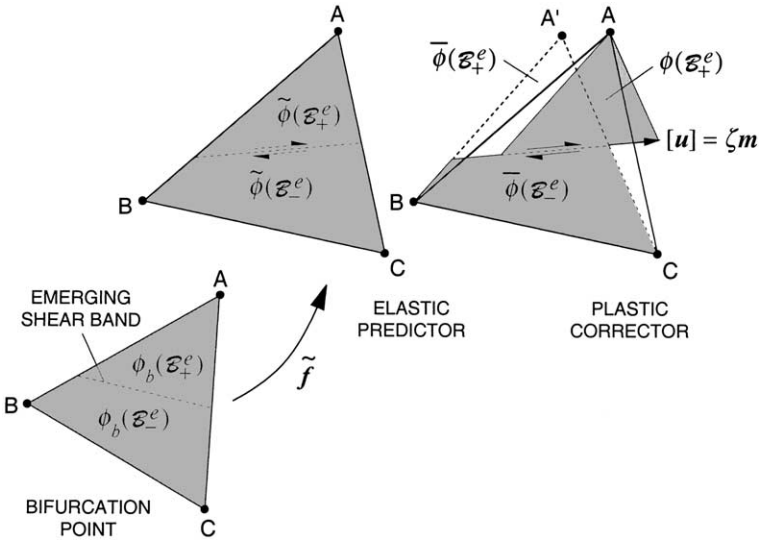

Fig. 3. Elastic predictor–plastic corrector algorithm for a localized CST element. Note: shaded region denotes total configuration, triangle ABC = conforming configuration, triangle A′BC = continuous configuration.

$$-r'(\Delta\zeta) = \boldsymbol{g} : \boldsymbol{a} + \widetilde{\mathscr{H}}_\delta, \tag{3.38}$$

where

$$\boldsymbol{a} = -\frac{\partial \boldsymbol{\tau}}{\partial \boldsymbol{b}^{\mathrm{e}}} : \frac{\partial \boldsymbol{b}^{\mathrm{e}}}{\partial \Delta\zeta} = -\boldsymbol{\alpha}^{\mathrm{e}} : \left(\frac{\partial \bar{\boldsymbol{f}}}{\partial \Delta\zeta} \cdot \bar{\boldsymbol{f}}^{-1} \right), \quad \boldsymbol{g} = \frac{\partial \mathscr{G}_{n+1}}{\partial \boldsymbol{\tau}}. \tag{3.39}$$

The above expression for $\boldsymbol{a}$ has been obtained from the derivative

$$\frac{\partial \boldsymbol{b}^{\mathrm{e}}}{\partial \Delta\zeta} = \frac{\partial \bar{\boldsymbol{f}}}{\partial \Delta\zeta} \cdot \bar{\boldsymbol{f}}^{-1} \cdot \boldsymbol{b}^{\mathrm{e}} + \boldsymbol{b}^{\mathrm{e}} \cdot \bar{\boldsymbol{f}}^{-t} \cdot \frac{\partial \bar{\boldsymbol{f}}^t}{\partial \Delta\zeta}, \tag{3.40}$$

where $\boldsymbol{b}^{\mathrm{e}}$ and the stress-deformation tangent operator $\boldsymbol{\varphi} = 2\partial\boldsymbol{\tau}/\partial\boldsymbol{b}^{\mathrm{e}}$ have been combined to produce the tangent operator $\boldsymbol{\alpha}^{\mathrm{e}}$, see (2.13). The remaining derivatives are readily obtained as

$$\frac{\partial \bar{\boldsymbol{f}}}{\partial \Delta\zeta} = -\frac{1}{1-\zeta_n \beta_n} \boldsymbol{m} \otimes \frac{\partial f^h}{\partial \widetilde{\boldsymbol{x}}_n}, \tag{3.41}$$

$$\frac{\partial \bar{\boldsymbol{f}}}{\partial \Delta\zeta} \cdot \bar{\boldsymbol{f}}^{-1} = -\frac{1}{1-\zeta\beta} \boldsymbol{m} \otimes \frac{\partial f^h}{\partial \widetilde{\boldsymbol{x}}} \equiv \frac{\partial \overline{\boldsymbol{F}}}{\partial \Delta\zeta} \cdot \overline{\boldsymbol{F}}^{-1}, \tag{3.42}$$

and so,

$$\boldsymbol{a} = \frac{1}{1-\zeta\beta} \boldsymbol{\alpha}^{\mathrm{e}} : \left(\boldsymbol{m} \otimes \frac{\partial f^h}{\partial \widetilde{\boldsymbol{x}}} \right). \tag{3.43}$$

The algorithm is summarized in Box 1. Some striking similarities with the general return mapping algorithm of continuum plasticity are readily noted. First, the incremental slip $\Delta\zeta = \zeta - \zeta_n$ plays the role of the discrete plastic multiplier, and the vector direction $\boldsymbol{m}$ plays the role of the return direction. The conforming configuration defined by the relative deformation gradient $\widetilde{\boldsymbol{f}}$ is held fixed during the course of the

iteration, much like the trial elastic strain in continuum plasticity, while the relative deformation gradient $\bar{\boldsymbol{f}}$ takes the role of the final elastic strain. Since the return direction $\boldsymbol{m}$ is fixed during the course of the iteration, the local Newton iteration only involves a scalar unknown (i.e., ζ). Finally, since $\boldsymbol{m}$ is determined exactly from the push-forward transformation of the fixed vector $\boldsymbol{M}$, the return direction is exact and there is no numerical approximation involved anywhere. In other words, the proposed overall stress-point integration algorithm is *exact*.

Box 1. Local Newton iteration algorithm for updating stresses in a traced element

Given $\tilde{\boldsymbol{f}}$, $\boldsymbol{b}^{\mathrm{e}}_n$, $\tau_{y,n}$, ζ_n; find $\boldsymbol{b}^{\mathrm{e}}$, τ_y, ζ:
Step 1. Compute $\boldsymbol{m} = \widetilde{\boldsymbol{F}} \cdot \boldsymbol{M} / \|\widetilde{\boldsymbol{F}} \cdot \boldsymbol{M}\|$.
Step 2. Set $\zeta = \zeta_n$; $\bar{\boldsymbol{f}} = \bar{\boldsymbol{f}}^{\mathrm{tr}}$; $\boldsymbol{b}^{\mathrm{e}} = \boldsymbol{b}^{\mathrm{e}\,\mathrm{tr}}$; $\boldsymbol{\tau} = \boldsymbol{\tau}^{\mathrm{tr}}$.
Step 3. $\mathscr{G}(\boldsymbol{\tau}^{\mathrm{tr}}, \tau_{y,n}) \leqslant 0$? Yes: Accept $\boldsymbol{b}^{\mathrm{e}}$ and exit.
Step 4. No: Initialize $\zeta = \zeta_n$; $\tau_y = \tau_{y,n}$.
Step 5. Calculate $\bar{\boldsymbol{f}}$, $\boldsymbol{b}^{\mathrm{e}}$, $\boldsymbol{\tau}$, and $r(\zeta) = \mathscr{G}(\boldsymbol{\tau}, \tau_y)$.
Step 6. $|r(\zeta)| < \mathrm{TOL}$? Yes: Accept $\boldsymbol{b}^{\mathrm{e}}$, τ_y, ζ and exit.
Step 7. No: Compute $\delta\zeta = -r(\zeta)/r'(\zeta)$.
Step 8. $\zeta \leftarrow \zeta + \delta\zeta$; $\tau_y = \tau_{y,n} + \Delta\tau_y$; and go to Step 5.

3.3. Algorithmic/continuum tangent operator

The algorithmic tangent operator for a typical localized or damaged element $\mathscr{B}^{\mathrm{e}}$ is based on a consistent linearization of the variational equations (3.1) and (3.2). As noted earlier, the proposed stress-point integration algorithm is exact, and so the algorithmic tangent operator is the same as the continuum overall tangent operator. Let us then take the first variation of (3.2) as follows:

$$\delta W^{\mathrm{e}}_{\mathrm{INT}} = \delta \int_{\mathscr{B}^{\mathrm{e}}} \mathrm{GRAD}\,\boldsymbol{\eta} : \boldsymbol{P}\,\mathrm{d}V = \int_{\mathscr{B}^{\mathrm{e}}} \mathrm{GRAD}\,\boldsymbol{\eta} : (\delta\boldsymbol{\tau} \cdot \overline{\boldsymbol{F}}^{-t} + \boldsymbol{\tau} \cdot \delta\overline{\boldsymbol{F}}^{-t})\,\mathrm{d}V. \tag{3.44}$$

Recalling that

$$\delta\boldsymbol{\tau} = \boldsymbol{\alpha}^{\mathrm{e}} : \bar{\mathrm{g}}\mathrm{rad}\,\delta\bar{\boldsymbol{u}}, \quad \delta\overline{\boldsymbol{F}}^{-1} = -\overline{\boldsymbol{F}}^{-1} \cdot \bar{\mathrm{g}}\mathrm{rad}\,\delta\bar{\boldsymbol{u}}, \tag{3.45}$$

we obtain the following expression for the first variation of the element internal virtual work:

$$\delta W^{\mathrm{e}}_{\mathrm{INT}} = \int_{\mathscr{B}^{\mathrm{e}}} \bar{\mathrm{g}}\mathrm{rad}\,\boldsymbol{\eta} : (\delta\boldsymbol{\tau} - \delta\boldsymbol{\tau}')\mathrm{d}V = \int_{\mathscr{B}^{\mathrm{e}}} \bar{\mathrm{g}}\mathrm{rad}\,\boldsymbol{\eta} : \mathbf{a}^{\mathrm{e}} : \bar{\mathrm{g}}\mathrm{rad}\,\delta\bar{\boldsymbol{u}}\,\mathrm{d}V, \quad \mathbf{a}^{\mathrm{e}} = \boldsymbol{\alpha}^{\mathrm{e}} - \boldsymbol{\tau} \ominus \mathbf{1}, \tag{3.46}$$

where $(\boldsymbol{\tau} \ominus \mathbf{1})_{ijkl} = \tau_{il}\delta_{jk}$ and $\delta\boldsymbol{\tau}' = (\boldsymbol{\tau} \ominus \mathbf{1}) : \bar{\mathrm{g}}\mathrm{rad}\,\delta\bar{\boldsymbol{u}}$ represents the stress contribution to the variation. An alternative expression for the first variation utilizes a material description and takes the form

$$\delta W^{\mathrm{e}}_{\mathrm{INT}} = \int_{\mathscr{B}^{\mathrm{e}}} \mathrm{GRAD}\,\boldsymbol{\eta} : \overline{\mathbf{A}}^{\mathrm{e}} : \mathrm{GRAD}\,\delta\bar{\boldsymbol{u}}\,\mathrm{d}V, \quad \bar{\mathsf{A}}^{\mathrm{e}}_{iAjB} = \overline{F}^{-1}_{Aj}\overline{F}^{-1}_{Bl}\mathsf{a}^{\mathrm{e}}_{ikjl}. \tag{3.47}$$

The latter expression is less natural to use, and as pointed out earlier we shall focus instead on the spatial form (3.46). It must be noted, however, that the quantities appearing in the expressions above all describe the continuous part of motion. Our goal is to reformulate the first variation of $W^{\mathrm{e}}_{\mathrm{INT}}$ into a more standard finite element format that utilizes the conforming part of motion.

Let us rewrite the first variation of the Kirchhoff stress tensor in the form

$$\delta\boldsymbol{\tau} = \boldsymbol{\alpha}^{\mathrm{e}} : \bar{\mathrm{g}}\mathrm{rad}\,\delta\bar{\boldsymbol{u}} = \boldsymbol{\alpha}^{\mathrm{e}} : (\delta\bar{\boldsymbol{f}} \cdot \bar{\boldsymbol{f}}^{-1}) = \boldsymbol{\alpha}^{\mathrm{e}} : (\delta\overline{\boldsymbol{F}} \cdot \overline{\boldsymbol{F}}^{-1}). \tag{3.48}$$

The first variation of $\overline{\boldsymbol{F}}$ from (3.12), second part, is given by

$$\delta\overline{\boldsymbol{F}} = \delta\widetilde{\boldsymbol{F}} - (\zeta\,\delta\boldsymbol{m} + \delta\zeta\,\boldsymbol{m}) \otimes \frac{\partial f^h}{\partial \boldsymbol{X}}. \tag{3.49}$$

Note that $\delta\overline{\boldsymbol{F}} \neq \delta\widetilde{\boldsymbol{F}}$ even if $\delta\zeta = 0$ since the slip magnitude ζ is transformed by the motion, i.e., $\delta\boldsymbol{m} \neq \boldsymbol{0}$. The first variation of $\boldsymbol{m} = \widetilde{\boldsymbol{F}} \cdot \boldsymbol{M}/\|\widetilde{\boldsymbol{F}} \cdot \boldsymbol{M}\|$ requires the first variation

$$\delta\widetilde{\boldsymbol{F}} = \widetilde{\mathrm{g}}\mathrm{rad}\,\delta\widetilde{\boldsymbol{u}} \cdot \widetilde{\boldsymbol{F}}, \tag{3.50}$$

where $\widetilde{\mathrm{g}}\mathrm{rad}(\cdot) = \partial(\cdot)/\partial\widetilde{\boldsymbol{x}}$. From the chain rule, we thus get

$$\delta\boldsymbol{m} = \widetilde{\mathrm{g}}\mathrm{rad}\,\delta\widetilde{\boldsymbol{u}} \cdot \boldsymbol{m} - [\widetilde{\mathrm{g}}\mathrm{rad}\,\delta\widetilde{\boldsymbol{u}} : (\boldsymbol{m} \otimes \boldsymbol{m})]\boldsymbol{m}. \tag{3.51}$$

The obvious orthogonality condition $\boldsymbol{m} \cdot \delta\boldsymbol{m} = 0$ is readily recovered from the above result following the normalization $\|\boldsymbol{m}\| = 1$.

Utilizing the expression (3.20) for the inverse $\overline{\boldsymbol{F}}^{-1}$, and after some mathematical manipulations, we obtain

$$\delta\overline{\boldsymbol{F}} \cdot \overline{\boldsymbol{F}}^{-1} = \widetilde{\mathrm{g}}\mathrm{rad}\,\delta\widetilde{\boldsymbol{u}} + \frac{\zeta}{1-\zeta\beta}[\widetilde{\mathrm{g}}\mathrm{rad}\,\delta\widetilde{\boldsymbol{u}} : (\boldsymbol{m} \otimes \boldsymbol{m})]\boldsymbol{m} \otimes \frac{\partial f^h}{\partial \widetilde{\boldsymbol{x}}} - \frac{\delta\zeta}{1-\zeta\beta}\boldsymbol{m} \otimes \frac{\partial f^h}{\partial \widetilde{\boldsymbol{x}}}. \tag{3.52}$$

This leads to the following expression for the first variation of the Kirchhoff stress tensor:

$$\delta\boldsymbol{\tau} = \boldsymbol{\alpha}^{\mathrm{e}} : \widetilde{\mathrm{g}}\mathrm{rad}\,\delta\widetilde{\boldsymbol{u}} + \frac{\zeta}{1-\zeta\beta}[\widetilde{\mathrm{g}}\mathrm{rad}\,\delta\widetilde{\boldsymbol{u}} : \boldsymbol{m} \otimes \boldsymbol{m})]\boldsymbol{\alpha}^{\mathrm{e}} : \left(\boldsymbol{m} \otimes \frac{\partial f^h}{\partial \widetilde{\boldsymbol{x}}}\right) - \frac{\delta\zeta}{1-\zeta\beta}\boldsymbol{\alpha}^{\mathrm{e}} : \left(\boldsymbol{m} \otimes \frac{\partial f^h}{\partial \widetilde{\boldsymbol{x}}}\right). \tag{3.53}$$

In the expressions above, we recall that $\delta\zeta = 0$ for a dormant shear band and $\delta\zeta > 0$ for an active shear band.

For an active shear band we have an additional consistency condition (3.36) to satisfy. Linearizing this equation gives

$$\delta\mathscr{G} = \boldsymbol{g} : \delta\boldsymbol{\tau} - \widetilde{\mathscr{H}}_{\delta}\,\delta\zeta = 0, \tag{3.54}$$

where $\boldsymbol{g} = \partial\mathscr{G}_{n+1}/\partial\boldsymbol{\tau}$. Inserting (3.53) into this condition and solving for $\delta\zeta$ yields

$$\delta\zeta = \frac{1}{\chi}\boldsymbol{g} : \boldsymbol{\alpha}^{\mathrm{e}} : \widetilde{\mathrm{g}}\mathrm{rad}\,\delta\widetilde{\boldsymbol{u}} + \frac{1}{\chi}\frac{\zeta}{1-\zeta\beta}[\widetilde{\mathrm{g}}\mathrm{rad}\,\delta\widetilde{\boldsymbol{u}} : (\boldsymbol{m} \otimes \boldsymbol{m})]\boldsymbol{g} : \boldsymbol{\alpha}^{\mathrm{e}} : \left(\boldsymbol{m} \otimes \frac{\partial f^h}{\partial \widetilde{\boldsymbol{x}}}\right), \tag{3.55}$$

where

$$\chi = \frac{1}{1-\zeta\beta}\boldsymbol{g} : \boldsymbol{\alpha}^{\mathrm{e}} : \left(\boldsymbol{m} \otimes \frac{\partial f^h}{\partial \widetilde{\boldsymbol{x}}}\right) + \widetilde{\mathscr{H}}_{\delta}. \tag{3.56}$$

Inserting back into (3.53) gives

$$\delta\boldsymbol{\tau} = \boldsymbol{\alpha}^{\mathrm{ep}} : \widetilde{\mathrm{g}}\mathrm{rad}\,\delta\widetilde{\boldsymbol{u}} + \frac{\zeta}{1-\zeta\beta}[\widetilde{\mathrm{g}}\mathrm{rad}\,\delta\widetilde{\boldsymbol{u}} : (\boldsymbol{m} \otimes \boldsymbol{m})]\boldsymbol{\alpha}^{\mathrm{ep}} : \left(\boldsymbol{m} \otimes \frac{\partial f^h}{\partial \widetilde{\boldsymbol{x}}}\right), \tag{3.57}$$

where

$$\boldsymbol{\alpha}^{\mathrm{ep}} = \boldsymbol{\alpha}^{\mathrm{e}} - \frac{\boldsymbol{a} \otimes \widetilde{\boldsymbol{a}}}{\boldsymbol{g} : \boldsymbol{a} + \widetilde{\mathscr{H}}_{\delta}}. \tag{3.58}$$

In this last equation, $\boldsymbol{a}$ is determined from (3.43) and $\widetilde{\boldsymbol{a}} = \boldsymbol{g} : \boldsymbol{\alpha}^{\mathrm{e}}$, cf. (3.10) of [24].

Next, let us rewrite the stress contribution $\delta\boldsymbol{\tau}'$ to the internal virtual work as

$$\delta\boldsymbol{\tau}' = (\boldsymbol{\tau} \ominus \boldsymbol{1}) : \bar{\mathrm{g}}\mathrm{rad}\,\delta\bar{\boldsymbol{u}} = (\boldsymbol{\tau} \ominus \boldsymbol{1}) : (\delta\bar{\boldsymbol{f}} \cdot \bar{\boldsymbol{f}}^{-1}) = (\boldsymbol{\tau} \ominus \boldsymbol{1}) : (\delta\overline{\boldsymbol{F}} \cdot \overline{\boldsymbol{F}}^{-1}). \tag{3.59}$$

Following the developments of (3.52) and (3.53), we get

$$\delta\boldsymbol{\tau}' = (\boldsymbol{\tau}\ominus\mathbf{1}) : \widetilde{\mathrm{grad}}\,\delta\widetilde{\boldsymbol{u}} + \frac{\zeta}{1-\zeta\beta}[\widetilde{\mathrm{grad}}\,\delta\widetilde{\boldsymbol{u}} : (\boldsymbol{m}\otimes\boldsymbol{m})](\boldsymbol{\tau}\ominus\mathbf{1}) : \left(\boldsymbol{m}\otimes\frac{\partial f^h}{\partial\widetilde{\boldsymbol{x}}}\right) - \frac{\delta\zeta}{1-\zeta\beta}(\boldsymbol{\tau}\ominus\mathbf{1}) : \left(\boldsymbol{m}\otimes\frac{\partial f^h}{\partial\widetilde{\boldsymbol{x}}}\right). \tag{3.60}$$

Substituting the expression (3.55) for $\delta\zeta$ gives

$$\delta\boldsymbol{\tau}' = \boldsymbol{\xi}^{\mathrm{ep}} : \widetilde{\mathrm{grad}}\,\delta\widetilde{\boldsymbol{u}} + \frac{\zeta}{1-\zeta\beta}[\widetilde{\mathrm{grad}}\,\delta\widetilde{\boldsymbol{u}} : (\boldsymbol{m}\otimes\boldsymbol{m})]\boldsymbol{\xi}^{\mathrm{ep}} : \left(\boldsymbol{m}\otimes\frac{\partial f^h}{\partial\widetilde{\boldsymbol{x}}}\right), \tag{3.61}$$

where

$$\boldsymbol{\xi}^{\mathrm{ep}} = \boldsymbol{\tau}\ominus\mathbf{1} - \frac{\boldsymbol{a}'\otimes\widetilde{\boldsymbol{a}}}{\boldsymbol{g}:\boldsymbol{a} + \widetilde{\mathscr{H}}_\delta} \tag{3.62}$$

and

$$\boldsymbol{a}' = \frac{1}{1-\zeta\beta}(\boldsymbol{\tau}\ominus\mathbf{1}) : \left(\boldsymbol{m}\otimes\frac{\partial f^h}{\partial\widetilde{\boldsymbol{x}}}\right). \tag{3.63}$$

Let us now subtract (3.61) from (3.57). The result reads

$$\delta\boldsymbol{\tau} - \delta\boldsymbol{\tau}' = \mathbf{a}^{\mathrm{ep}} : \widetilde{\mathrm{grad}}\,\delta\widetilde{\boldsymbol{u}} + \frac{\zeta}{1-\zeta\beta}[\widetilde{\mathrm{grad}}\,\delta\widetilde{\boldsymbol{u}} : (\boldsymbol{m}\otimes\boldsymbol{m})]\mathbf{a}^{\mathrm{ep}} : \left(\boldsymbol{m}\otimes\frac{\partial f^h}{\partial\widetilde{\boldsymbol{x}}}\right), \tag{3.64}$$

where

$$\mathbf{a}^{\mathrm{ep}} = \boldsymbol{\alpha}^{\mathrm{ep}} - \boldsymbol{\xi}^{\mathrm{ep}} = \mathbf{a}^{\mathrm{e}} - \frac{(\boldsymbol{a}-\boldsymbol{a}')\otimes\widetilde{\boldsymbol{a}}}{\boldsymbol{g}:\boldsymbol{a} + \widetilde{\mathscr{H}}_\delta} \tag{3.65}$$

and

$$\boldsymbol{a} - \boldsymbol{a}' = \frac{1}{1-\zeta\beta}\mathbf{a}^{\mathrm{e}} : \left(\boldsymbol{m}\otimes\frac{\partial f^h}{\partial\widetilde{\boldsymbol{x}}}\right), \tag{3.66}$$

with $\mathbf{a}^{\mathrm{e}} = \boldsymbol{\alpha}^{\mathrm{e}} - \boldsymbol{\tau}\ominus\mathbf{1}$ as before.

Finally, let us pull out the spatial gradient terms $\widetilde{\mathrm{grad}}\,\delta\widetilde{\boldsymbol{u}}$ to obtain the linearization

$$\delta\boldsymbol{\tau} - \delta\boldsymbol{\tau}' = \mathbf{a} : \widetilde{\mathrm{grad}}\,\delta\widetilde{\boldsymbol{u}}, \tag{3.67}$$

where

$$\mathbf{a} = \mathbf{a}^{\mathrm{ep}} + \frac{\zeta}{1-\zeta\beta}\mathbf{a}^{\mathrm{ep}} : \left(\boldsymbol{m}\otimes\frac{\partial f^h}{\partial\widetilde{\boldsymbol{x}}}\right)\otimes(\boldsymbol{m}\otimes\boldsymbol{m}) \tag{3.68}$$

is the overall algorithmic/continuum tangent operator. The plastic corrector component of $\mathbf{a}^{\mathrm{ep}}$ appearing in (3.65) results from the incremental plastic slip on the band, and for a dormant shear band this term reduces identically to zero, giving $\mathbf{a}^{\mathrm{ep}} = \mathbf{a}^{\mathrm{e}}$. The second component of the overall tangent operator $\mathbf{a}$ appearing in (3.68) arises from an objective transformation of the accumulated plastic slip ζ and vanishes identically when $\zeta = 0$.

On substitution of (3.68) into (3.46), we get the final form for the first variation of the internal virtual work

$$\delta W^{\mathrm{e}}_{\mathrm{INT}} = \int_{\mathscr{B}^{\mathrm{e}}} \bar{\mathrm{grad}}\,\boldsymbol{\eta} : \mathbf{a} : \widetilde{\mathrm{grad}}\,\delta\widetilde{\boldsymbol{u}}\,\mathrm{d}V. \tag{3.69}$$

The integral developed above has a structure of a Petrov–Galerkin formulation in that the gradient of the weighting function $\boldsymbol{\eta}$ and the gradient of the trial function $\delta\widetilde{\boldsymbol{u}}$ are evaluated over two distinct deformation configurations. The standard Galerkin approximation is recovered from this formulation when $\zeta = 0$, which occurs before and up to the moment of bifurcation. However, beyond the bifurcation point the conforming deformation map deviates away from the continuous deformation map with accumulating plastic slip on the band.

3.4. Finite element implementation

Determining the spatial gradients of the continuous map requires a very small incremental effort. Consider, for example, a standard finite element interpolation of the weighting function $\boldsymbol{\eta}$

$$\boldsymbol{\eta} = \sum_{A=1}^{n_{\text{en}}} N_A \boldsymbol{\eta}_A, \tag{3.70}$$

where $\boldsymbol{\eta}_A$ are the nodal values and N_A are standard finite element shape functions, with n_{en} being the number of nodes. The spatial gradient of the continuous map is then obtained as

$$\bar{\text{g}}\text{rad}\,\boldsymbol{\eta} = \frac{\partial \boldsymbol{\eta}}{\partial \bar{\boldsymbol{x}}} = \sum_{A=1}^{n_{\text{en}}} \frac{\partial N_A}{\partial \bar{\boldsymbol{x}}} \otimes \boldsymbol{\eta}_A = \sum_{A=1}^{n_{\text{en}}} \frac{\partial N_A}{\partial \boldsymbol{X}} \cdot \overline{\boldsymbol{F}}^{-1} \otimes \boldsymbol{\eta}_A. \tag{3.71}$$

Inserting the closed-form expression for the inverse of $\overline{\boldsymbol{F}}$ from (3.20), and after simplifying, we get

$$\bar{\text{g}}\text{rad}\,\boldsymbol{\eta} = \sum_{A=1}^{n_{\text{en}}} \left[\frac{\partial N_A}{\partial \widetilde{\boldsymbol{x}}} + \frac{\zeta}{1-\zeta\beta} \left(\frac{\partial N_A}{\partial \widetilde{\boldsymbol{x}}} \cdot \boldsymbol{m} \right) \frac{\partial f^h}{\partial \widetilde{\boldsymbol{x}}} \right] \otimes \boldsymbol{\eta}_A. \tag{3.72}$$

In other words, we have

$$\frac{\partial N_A}{\partial \bar{\boldsymbol{x}}} = \frac{\partial N_A}{\partial \widetilde{\boldsymbol{x}}} + \frac{\zeta}{1-\zeta\beta} \left(\frac{\partial N_A}{\partial \widetilde{\boldsymbol{x}}} \cdot \boldsymbol{m} \right) \frac{\partial f^h}{\partial \widetilde{\boldsymbol{x}}}, \tag{3.73}$$

where $\partial N_A/\partial \widetilde{\boldsymbol{x}}$ are the gradients of the standard shape functions with respect to the conforming map. Thus, the gradients of the shape functions with respect to the continuous map can be obtained from the gradients of the shape functions with respect to the conforming map through a simple additive vector correction in the direction of $\partial f^h/\partial \widetilde{\boldsymbol{x}}$.

The evolution of deformation for a typical CST element, starting from the undeformed configuration, is depicted in Fig. 4. Checks are done for possible bifurcation at the end of each loading step. If the element localizes, and if it lies in front of an active shear band, then it is enhanced with a slip degree of freedom that is eliminated on the material level. Note that no static condensation on the element level is required by the proposed approach.

The bifurcation analysis generally results in two possible slip surface orientations one of which is selected according to the algorithm described in the next paragraph. The eigenvectors determined from this stability analysis represent possible instantaneous directions of the emerging velocity jump, and may or may not be tangent to the band depending on the constitutive response of the continuum in the intact state. One of these eigenvectors is denoted by $\boldsymbol{m}'$ in Fig. 4. However, the evolution condition requires that the slip direction $\boldsymbol{m}$ be tangent to the band immediately *after* localization, implying that the eigenvector $\boldsymbol{m}'$ plays no role in the subsequent multiscale simulation.

To select the more critical shear band orientation from two possible solutions, we consider the push-forward transformations of two material vectors, one parallel to the tangent vector $\boldsymbol{M}$ and another parallel to the normal vector $\boldsymbol{N}$ in the undeformed configuration, see Fig. 4. Since the critical shear band orientation

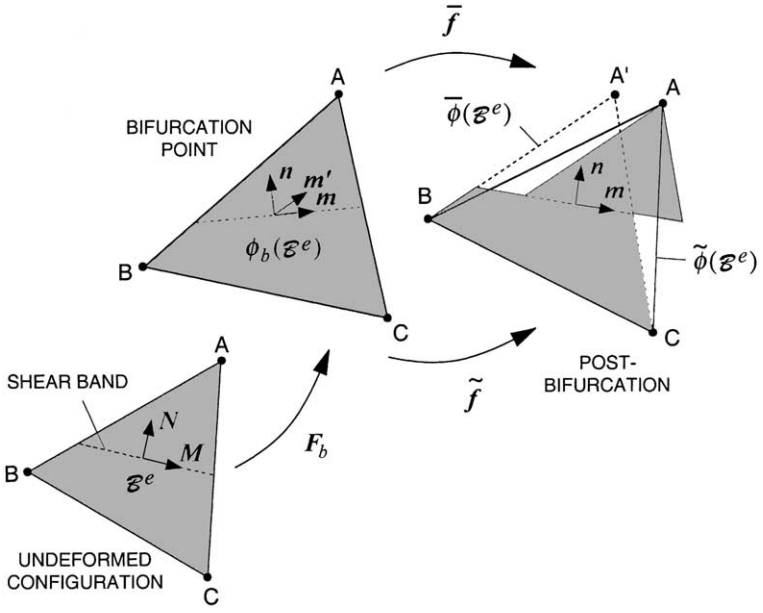

Fig. 4. Evolution of a CST element from undeformed configuration to bifurcation point and beyond.

should conform with the instantaneous deformation of the continuum at the moment of bifurcation, we select the shear band orientation that maximizes the scalar product

$$\theta = (\boldsymbol{F}_{\mathrm{b}} \cdot \boldsymbol{M}) \cdot (\boldsymbol{F}_{\mathrm{b}} \cdot \boldsymbol{N}), \tag{3.74}$$

where $\boldsymbol{F}_{\mathrm{b}}$ is the current deformation gradient at the moment of bifurcation. Now, since

$$\boldsymbol{M} = \boldsymbol{F}_{\mathrm{b}}^{-1} \cdot \boldsymbol{m} / ||\boldsymbol{F}_{\mathrm{b}}^{-1} \cdot \boldsymbol{m}||, \quad \boldsymbol{N} = \boldsymbol{n} \cdot \boldsymbol{F}_{\mathrm{b}} / ||\boldsymbol{n} \cdot \boldsymbol{F}_{\mathrm{b}}||, \tag{3.75}$$

where $\boldsymbol{m}$ and $\boldsymbol{n}$ are candidate tangent and cotangent spatial vectors determined from the bifurcation analysis, then the critical shear band orientation also can be chosen as the one that maximizes the scalar product

$$\theta' = (\boldsymbol{m} \cdot \boldsymbol{F}_{\mathrm{b}}) \cdot (\boldsymbol{n} \cdot \boldsymbol{F}_{\mathrm{b}}) = 2(\boldsymbol{m} \otimes \boldsymbol{n}) : \frac{\partial \boldsymbol{u}_{\mathrm{b}}}{\partial \boldsymbol{X}} + \left(\boldsymbol{m} \cdot \frac{\partial \boldsymbol{u}_{\mathrm{b}}}{\partial \boldsymbol{X}} \right) \cdot \left(\boldsymbol{n} \cdot \frac{\partial \boldsymbol{u}_{\mathrm{b}}}{\partial \boldsymbol{X}} \right), \tag{3.76}$$

where $\boldsymbol{u}_{\mathrm{b}}$ is the displacement field at the bifurcation point. In the limit of infinitesimal deformation the second-order term drops out, and this criterion reduces to the one proposed in [24].

The ramp function f^h is a critical component of the multiscale formulation, and its gradients represent the single most important information needed by the model to provide a truly objective, mesh-independent solution. We find it convenient to evaluate $\partial f^h / \partial \boldsymbol{X}$ once and for all, which are stored in the memory. The spatial gradients $\partial f^h / \partial \tilde{\boldsymbol{x}}_n$ and $\partial f^h / \partial \tilde{\boldsymbol{x}}$ can then be evaluated by using the inverses of the deformation gradients $\tilde{\boldsymbol{F}}_n$ and $\tilde{\boldsymbol{F}}$. Since a traced CST element always contains a one-node side and a two-node side, then the element shape function proposed in [34] may be used, which results in the gradient $\partial f^h / \partial \boldsymbol{X}$ being always perpendicular to the two-node side. Referring to Fig. 5, $\boldsymbol{K}^{\mathrm{e}} = (\boldsymbol{X}^* - \boldsymbol{X}_A)/h_0^{\mathrm{e}}$ is the outward unit normal vector to the two-node side of a CST element; hence, $\partial f^h / \partial \boldsymbol{X} = \pm \boldsymbol{K}^{\mathrm{e}} / h_0^{\mathrm{e}}$, where the appropriate sign is chosen so that $\boldsymbol{N} \cdot \partial f^h / \partial \boldsymbol{X} > 0$. Because the shear band is embedded in the element, the one-node and two-node sides always remain on the same sides no matter how much the element has deformed.

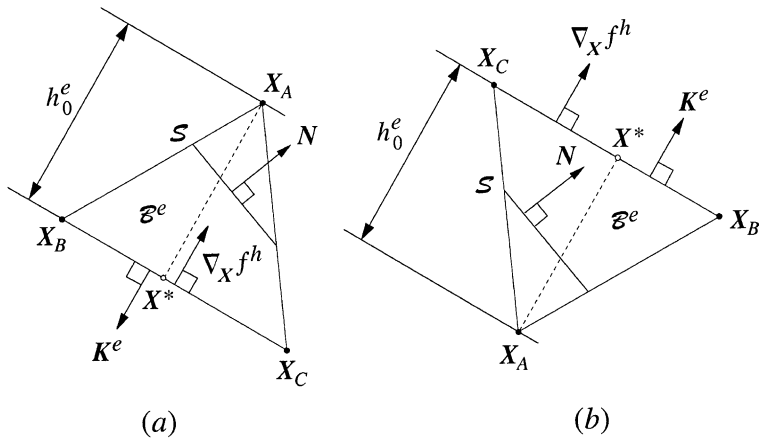

Fig. 5. Evaluation of ramp function gradient for CST element crossed by a shear band reckoned from the underformed configuration: (a) one-node side on the positive side of $\mathscr{S}$; (b) two-node side on the positive side of $\mathscr{S}$.

3.5. Embedded slip plane: yielding based on resolved shear stress

So far we have only considered a class of post-localized yield functions of the form $\mathscr{G} = \mathscr{G}(\boldsymbol{\tau}, \tau_y) = 0$ characterizing yielding of the material on the band. The Mises yield criterion formulated in Kirchhoff stress space is an example of such yield function,

$$\mathscr{G}(\boldsymbol{\tau}, \tau_y) = ||\boldsymbol{s}|| - \tau_y = 0, \quad \boldsymbol{s} = \boldsymbol{\tau} - \mathrm{tr}(\boldsymbol{\tau})\mathbf{1}/3. \tag{3.77}$$

From a physical standpoint, the use of this class of yield functions implies that the shear band is represented as an *embedded continuum* since the yield condition only depends on the continuum stresses inside a localizing element but not on the configuration of the shear band inside this element.

In a true strong discontinuity, it may be argued that such class of continuum yield models no longer applies. For example, consider a shear band on the plane $(1,2)$ normal to which the stress component τ_{33} acts. If the shear band thickness is zero, then there is no shear band area on which τ_{33} can possibly act, and so it may be argued that yielding of the material "inside the band" cannot possibly depend on τ_{33} due to the loss of dimension associated with strong discontinuity. In this case, an alternative yield criterion of the form $\mathscr{G} = \mathscr{G}(\boldsymbol{\tau}, \widetilde{\boldsymbol{F}}, \tau_y) = 0$ may be assumed to describe the plastic slips occurring on the surface of discontinuity. Thus, the shear band here is an *embedded slip plane* and the strong discontinuity acts like a 'glide plane' of crystal plasticity [42].

A specific yield criterion pursued in this work is based on the resolved shear stress on the band, and takes the form

$$\mathscr{G}(\boldsymbol{\tau}, \widetilde{\boldsymbol{F}}, \bar{c}) = (\boldsymbol{n} \otimes \boldsymbol{\mu}) : \boldsymbol{\tau} - \bar{c} = 0, \quad \boldsymbol{\mu} = \boldsymbol{m} + \boldsymbol{n}\tan\bar{\phi}, \tag{3.78}$$

where $\bar{\phi}$ and $\bar{c}$ are the mobilized friction angle and cohesion on the surface of discontinuity, respectively, and $\boldsymbol{m}$ and $\boldsymbol{n}$ are the spatial tangent and normal vectors to the shear band. Here, the deformation gradient $\widetilde{\boldsymbol{F}}$ enters into the yield criterion through the vectors $\boldsymbol{m}$ and $\boldsymbol{n}$.

Introducing the additional kinematical variable $\widetilde{\boldsymbol{F}}$ into the yield criterion $\mathscr{G}$ does not affect the formulation for the local iteration algorithm, as may be seen from Box 1, since $\boldsymbol{m}$ and $\boldsymbol{n}$ remain fixed during the course of the local iteration. However, it impacts the discrete consistency condition (3.36) for the global iteration, since its exact linearization now writes

$$\delta\mathscr{G} = \boldsymbol{g} : \delta\boldsymbol{\tau} + \boldsymbol{h} : \delta\widetilde{\boldsymbol{F}} - \widetilde{\mathscr{H}}_{\delta}\delta\zeta = 0, \tag{3.79}$$

where $\boldsymbol{g} = \partial\mathscr{G}_{n+1}/\partial\boldsymbol{\tau}$ and $\boldsymbol{h} = \partial\mathscr{G}_{n+1}/\partial\widetilde{\boldsymbol{F}}$. In the limit of infinitesimal deformation the additional term $\boldsymbol{h} : \delta\widetilde{\boldsymbol{F}}$ drops out, see [24], but in finite deformation calculations ignoring this term could lead to a loss of quadratic convergence in Newton iterations.

Noting that the first variation of $\boldsymbol{n} = \boldsymbol{N}\cdot\widetilde{\boldsymbol{F}}^{-1}/||\boldsymbol{N}\cdot\widetilde{\boldsymbol{F}}^{-1}||$ is

$$\delta\boldsymbol{n} = -\boldsymbol{n}\cdot\widetilde{\mathrm{grad}}\,\delta\widetilde{\boldsymbol{u}} + \boldsymbol{n}[(\boldsymbol{n}\otimes\boldsymbol{n}) : \widetilde{\mathrm{grad}}\,\delta\widetilde{\boldsymbol{u}}], \tag{3.80}$$

and using (3.45) and (3.50), we obtain (after skipping some details)

$$\boldsymbol{h} : \delta\widetilde{\boldsymbol{F}} = \overset{\nabla}{\boldsymbol{\tau}} : \widetilde{\mathrm{grad}}\,\delta\widetilde{\boldsymbol{u}}, \tag{3.81}$$

where

$$\overset{\nabla}{\boldsymbol{\tau}} = \boldsymbol{t}_n\otimes\boldsymbol{m} - \tau_{nm}\boldsymbol{m}\otimes\boldsymbol{m} - \tan\bar{\phi}\boldsymbol{n}\otimes\boldsymbol{t}_n + \tau_{nn}\tan\bar{\phi}\boldsymbol{n}\otimes\boldsymbol{n} - \boldsymbol{n}\otimes\boldsymbol{t}_{\mu} + \tau_{n\mu}\boldsymbol{n}\otimes\boldsymbol{n}, \tag{3.82}$$

and where we have used the symbols

$$\tau_{nn} = \boldsymbol{\tau} : (\boldsymbol{n}\otimes\boldsymbol{n}), \quad \tau_{nm} = \boldsymbol{\tau} : (\boldsymbol{n}\otimes\boldsymbol{m}), \quad \tau_{n\mu} = \boldsymbol{\tau} : (\boldsymbol{n}\otimes\boldsymbol{\mu}), \quad \boldsymbol{t}_n = \boldsymbol{n}\cdot\boldsymbol{\tau} = \boldsymbol{\tau}\cdot\boldsymbol{n},$$
$$\boldsymbol{t}_{\mu} = \boldsymbol{\tau}\cdot\boldsymbol{\mu} = \boldsymbol{\mu}\cdot\boldsymbol{\tau}. \tag{3.83}$$

With these extra terms, the first variation of the plastic multiplier now takes the form

$$\delta\zeta \leftarrow \delta\zeta + \frac{1}{\chi}\overset{\nabla}{\boldsymbol{\tau}} : \widetilde{\mathrm{grad}}\,\delta\widetilde{\boldsymbol{u}}, \tag{3.84}$$

while the first variations of the stresses become

$$\delta\boldsymbol{\tau} - \delta\boldsymbol{\tau}' \leftarrow (\delta\boldsymbol{\tau} - \delta\boldsymbol{\tau}') - \frac{1}{\chi(1-\zeta\beta)}\mathbf{a}^{\mathrm{e}} : \left(\boldsymbol{m}\otimes\frac{\partial f^h}{\partial\widetilde{\boldsymbol{x}}}\right)\otimes\overset{\nabla}{\boldsymbol{\tau}} : \widetilde{\mathrm{grad}}\,\delta\widetilde{\boldsymbol{u}}. \tag{3.85}$$

Finally, the algorithmic/continuum tangent operator changes to

$$\mathbf{a} \leftarrow \mathbf{a} - \frac{1}{\chi(1-\zeta\beta)}\mathbf{a}^{\mathrm{e}} : \left(\boldsymbol{m}\otimes\frac{\partial f^h}{\partial\widetilde{\boldsymbol{x}}}\right)\otimes\overset{\nabla}{\boldsymbol{\tau}}, \tag{3.86}$$

where the symbol '$\leftarrow$' suggests that the corresponding additional terms must be added to or subtracted from the expressions derived in Section 3.3. Note that these additional corrections are incorporated only for purposes of obtaining an exact linearization of the momentum balance equation and thus preserve the asymptotic quadratic rate of convergence of the global Newton iteration.

4. Numerical examples

In this section we present two numerical examples demonstrating objectivity with respect to mesh refinement and insensitivity to element alignment of finite element solutions employing the proposed multiscale modeling approach. We emphasize that in a general setting a truly mesh-independent solution does not exist since even the standard finite element solution exhibits some mesh dependency. However, under special circumstances a truly mesh-independent solution is possible, and in multiscale modeling this can be achieved if: (a) the standard finite element solution in the pre-localized state is truly mesh independent, which is possible if the mesh is subjected to a homogeneous state of stress prior to localization; (b) localization of all the elements in the mesh occurs at the same time, which follows directly from having a homogeneous state of stress at pre-localization; and (c) the band is completely traced in one time step, a

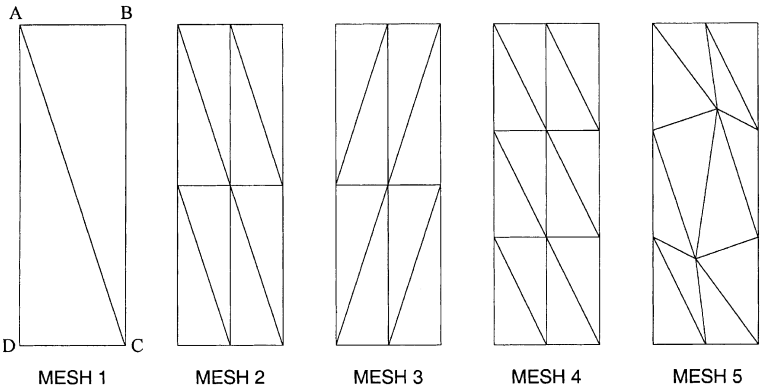

Fig. 6. Macrofinite element meshes for plane strain extension and compression examples.

reasonable proposition considering that all the elements are assumed to localize at the same time. Once localization takes place the band theoretically can emerge at any point in the mesh, although at this point it is important to select a band that is not inhibited to grow by any boundary constraint. Thus we can simply specify a point through which a specific band of interest passes. This latter technique is somewhat equivalent to specifying a weak element in the mesh, except that the latter approach perturbs the homogeneous state of stress and does not quite result in a truly mesh-independent solution.

The numerical examples involve plane strain extension and plane strain compression simulations on a hyperelastic–plastic solid deforming at finite strain. Fig. 6 shows five macroscale finite element meshes of varying mesh refinement and element alignment. The meshes are 3 m tall and 1 m wide, with a corner node D pinned to the base and the rest of the top and bottom nodes supported on vertical roller supports. Computations were done on a PC with a 16-digit double precision, which was sufficient for smaller meshes such as the ones shown in Fig. 6. Larger meshes may require higher precision calculations (such as a 32-digit machine precision), but this was deemed unnecessary for now since our objective is simply to demonstrate absolute objectivity of the solutions and not to analyze a large-scale boundary value problem. The material was represented by a quadratic logarithmic Drucker–Prager model described in [30], with a stored energy function that is quadratic in the principal elastic logarithmic stretches.

4.1. Plane strain extension simulations

In these simulations the top roller supports were moved uniformly upward in increments of 0.01 m while allowing both the top and bottom nodes to displace laterally (except the pinned node D), thus preserving a homogeneous state of stress up until the moment of bifurcation. The material parameters were as follows: hyperelastic Young's modulus $E = 500$ kPa and Poisson's ratio $\nu = 0.40$; the friction and dilatancy angles of the pre-localized Drucker–Prager model were set to zero, thus capturing a Von Mises plasticity with a pre-localized cohesion of 15 kPa and a pre-localized plastic modulus $H = 0$ (perfect plasticity). A slip plane was embedded at post-bifurcation, with a mobilized friction angle on the band $\bar{\phi} = 0$ (frictionless, purely cohesive) and a softening modulus $\tilde{\mathscr{H}}_\delta = -40$ kN/m.

The bifurcation point was detected at a total vertical displacement of 0.28 m, and as mentioned earlier an infinite number of shear bands is possible after localization. For analysis purposes the shear bands traced for each of the five meshes are shown in Fig. 7, all reckoned with respect to the undeformed configuration. Fig. 8 shows the deformation of Mesh#4 at the moment of bifurcation and at the conclusion of the simulation. An Eulerian bifurcation analysis predicted an orientation of the unit normal vector $\boldsymbol{n}$ at 44° to the

horizontal, which, by Nanson's formula, is equivalent to a pull-back orientation of the unit normal vector $\boldsymbol{N}$ at 49° from the horizontal. Note that the orientation of $\boldsymbol{n}$ is not quite equal to the value of 45° predicted by the small-strain theory because of the additional stress-term contributions to the acoustic tensor.

The predicted vertical load-vertical displacement curve is shown in Fig. 9. Predictions of the five meshes are identical to machine precision, as corroborated further in Table 1 which shows the calculated numerical values of the final displacements of corner nodes A, B, and C, as well as the calculated final cohesions and final accumulated slips at the conclusion of the simulations. Slips and cohesions across all traced elements were uniform, as expected. In Fig. 9, the elastic portion of the load–displacement response slightly curves downwards, and the apparent yield strength of the perfectly plastic region shows a slight decrease due to geometric effects as the effective loading area of the specimen decreases with increasing vertical elongation.

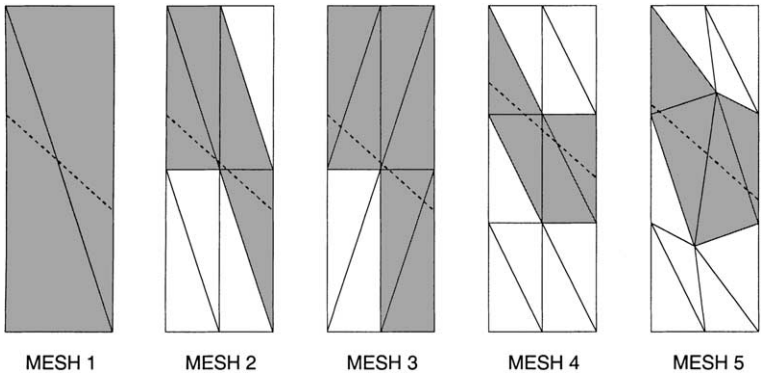

Fig. 7. Shear bands (dashed lines) and traced finite elements (shaded regions) for plane strain extension example.

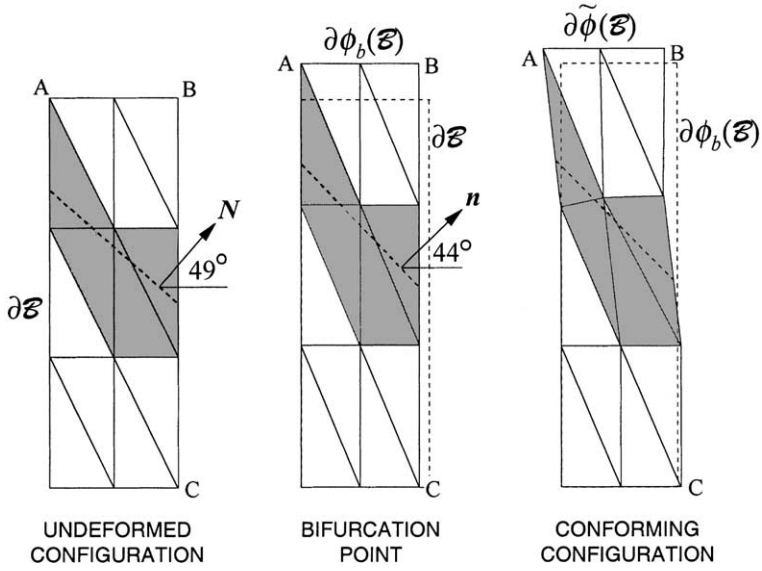

Fig. 8. Shear band initiation and evolution for plane strain extension example: displacement magnification factor = 1.

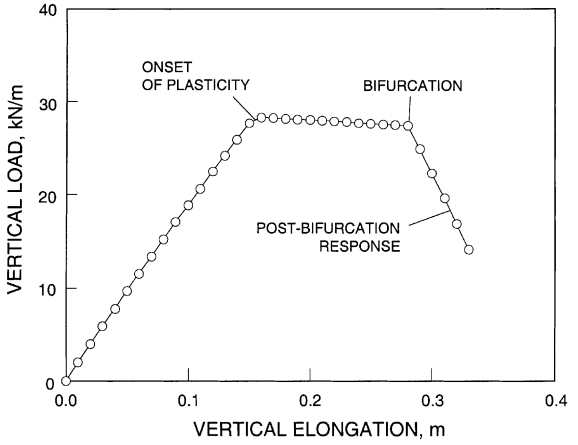

Fig. 9. Load–displacement curve for plane strain extension example.

Table 1
Numerical values of final displacements at corner nodes, final cohesion and final accumulated slip at end of plane strain extension simulation with embedded slip plane (total vertical elongation = 0.33 m)

	Mesh 1	Mesh 2	Mesh 3	Mesh 4	Mesh 5
u_x(A) (m)	−0.131970	−0.131970	−0.131970	−0.131970	−0.131970
u_x(B) (m)	−0.185585	−0.185585	−0.185585	−0.185585	−0.185585
u_x(C) (m)	−0.053615	−0.053615	−0.053615	−0.053615	−0.053615
Cohesion $\bar{c}$ (kPa)	7.531795	7.531795	7.531795	7.531795	7.531795
Slip ζ (m)	0.186003	0.186003	0.186003	0.186003	0.186003

4.2. Plane strain compression simulations

In these simulations the top roller supports were moved uniformly downward in increments of 0.01 m while allowing the top and bottom nodes to displace laterally (except node D). The material parameters were as follows: hyperelastic Young's modulus $E = 500$ kPa and Poisson's ratio $\nu = 0.40$; Drucker–Prager friction parameter $\beta = 0.495$ and dilatancy parameter $b = 0.30$ (nonassociative flow rule); pre-localized plastic modulus $H = 10$ kPa (hardening). An embedded Von Mises continuum and an embedded slip plane were both tested at post-bifurcation, with a mobilized friction angle on the band $\bar{\phi} = 0$ (frictionless, purely cohesive) for the embedded slip plane case, and a softening modulus $\widetilde{\mathscr{H}}_\delta = -55$ kN/m for both the embedded continuum and embedded slip plane cases.

The bifurcation point was detected at a total vertical displacement of −0.40 m, and compression was stopped at a total final vertical displacement of −0.49 m. Fig. 10 shows the shear bands traced for each of the five meshes, again reckoned with respect to the undeformed configuration. Fig. 11 shows the deformations of Mesh#4 at the bifurcation point and at the conclusion of the simulation. An Eulerian bifurcation analysis predicted an orientation of the vector $\boldsymbol{n}$ at 37° to the horizontal, or a pull-back orientation of the vector $\boldsymbol{N}$ at 30° to the horizontal.

The load–displacement curves predicted by the multiscale model are shown in Fig. 12 for both the embedded Von Mises continuum and the embedded slip plane cases discussed in Section 3.5. The apparent stiffening elastic response is again due to geometric effects as the effective loading area of the specimen increases with vertical compression. Note that bifurcation was detected in the hardening region, a possible

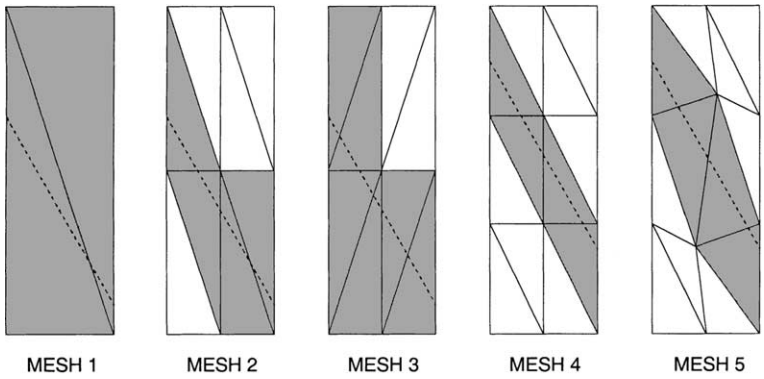

Fig. 10. Shear bands (dashed lines) and traced finite elements (shaded regions) for plane strain compression example.

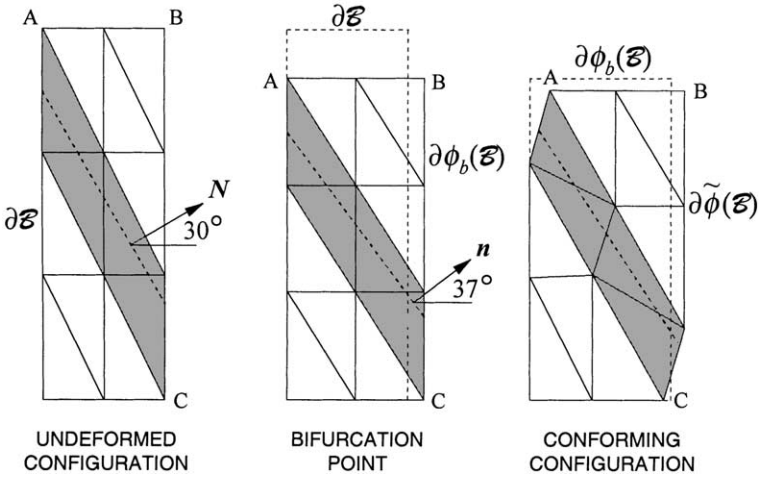

Fig. 11. Shear band initiation and evolution for plane strain compression example: displacement magnification factor = 1.

outcome with a nonassociated plasticity model particularly with the inclusion of geometric nonlinearities which tend to further enhance strain localization. Once again, the predictions from the five meshes were identical to machine precision as corroborated further by the calculated numerical values shown in Table 2.

As mentioned previously the stress-point integration algorithm at post-bifurcation is exact, and this is illustrated in Table 3 which reports the final values of the calculated cohesion and accumulated slip across the traced elements at the conclusion of the multiscale simulations. The table shows that the final values of the state variables are the same regardless of the number of load increments used. Note that the term "cohesion" here takes on the meaning of $\bar{c} = ||\boldsymbol{s}||$ for the Von Mises embedded continuum example, and $\bar{c} = \boldsymbol{\tau} : (\boldsymbol{m} \otimes \boldsymbol{n})$ for the embedded slip plane model, and so the two sets of values may not be compared one-on-one. Also, note that the starting point of the accuracy analysis calculations shown in Table 3 must be the same bifurcation point since the pre-localized stress-point integration algorithm is not exact.

The convergence profiles of both the local and global Newton iterations are shown in Tables 4 and 5 for the embedded Von Mises continuum example and the embedded slip plane case, respectively. These profiles

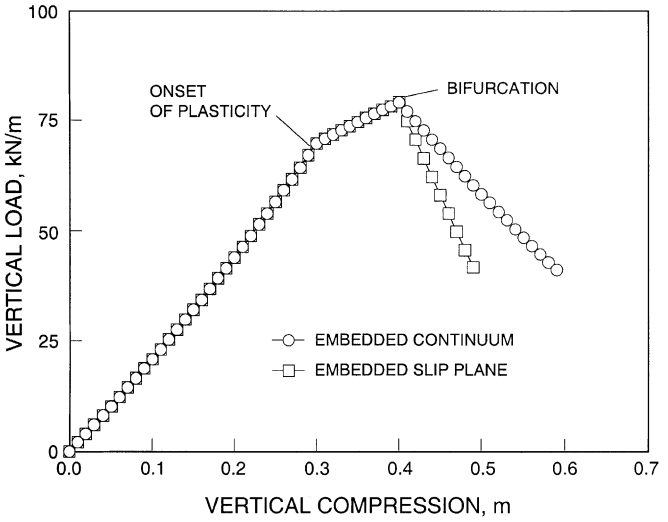

Fig. 12. Load–displacement curves for plane strain compression example using embedded continuum and embedded slip plane approaches.

Table 2
Numerical values of final displacements at corner nodes, final cohesion, and final accumulated slip at end of plane strain compression simulation with embedded slip plane (total vertical compression = 0.49 m)

	Mesh 1	Mesh 2	Mesh 3	Mesh 4	Mesh 5
u_x(A) (m)	0.157099	0.157099	0.157099	0.157099	0.157099
u_x(B) (m)	0.252852	0.252852	0.252852	0.252852	0.252852
u_x(C) (m)	0.095754	0.095754	0.095754	0.095754	0.095754
Cohesion $\bar{c}$ (kPa)	17.760723	17.760723	17.760723	17.760723	17.760723
Slip ζ (m)	0.276160	0.276160	0.276160	0.276160	0.276160

Table 3
Accuracy analyses for plane strain compression example: Mesh 1 with embedded continuum and embedded slip plane

	Number of load increments		
	1	10	40
Embedded continuum			
Cohesion $\bar{c}$ (kPa)	37.894533	37.894533	37.894533
Slip ζ (m)	0.192704	0.192704	0.192704
Embedded slip plane			
Cohesion $\bar{c}$ (kPa)	[a]	17.760723	17.760723
Slip ζ (m)	[a]	0.276160	0.276160

Note: number of imposed displacement increments are reckoned from bifurcation point.
[a] Did not converge.

pertain to the very last load step of the numerical simulations to get an idea of the performance of the algorithm at the very advanced stages of shear band development. The rapid rate of convergence of the iterations validates the exact linearization procedure used for the example at hand.

Table 4
Convergence profile of Newton iteration for plane strain compression example: Mesh 1 with embedded continuum

(1)	(2)	(3)	(4)
1.00e + 0	**8.17e − 2**	**3.09e − 6**	**7.47e − 13**
1.00e + 0	1.00e + 0	1.00e + 0	1.00e + 0
1.17e − 2	9.23e − 3	9.17e − 3	9.16e − 3
1.47e − 6	8.54e − 7	8.41e − 7	8.41e − 7
1.8e − 13	3.5e − 13	4.2e − 13	3.3e − 13
–	–	–	–

Note: bold-faced numbers pertain to residual norms of global iterations; light-faced numbers pertain to local iterations.

Table 5
Convergence profile of Newton iteration for plane strain compression example: Mesh 1 with embedded slip plane

(1)	(2)	(3)	(4)
1.00e + 0	**1.15e − 2**	**1.77e − 7**	**7.72e − 13**
1.00e + 0	1.00e + 0	1.00e + 0	1.00e + 0
5.23e − 3	3.50e − 3	3.51e − 3	3.51e − 3
1.44e − 7	4.31e − 8	4.35e − 8	4.35e − 8
1.3e − 13	2.7e − 13	4.2e − 13	1.3e − 13
–	–	–	–

Note: bold-faced numbers pertain to residual norms of global iterations; light-faced numbers pertain to local iterations.

5. Closure

The multiscale finite element model proposed in this paper has been developed with a central goal that it be physically based. It is believed that with a formulation that clearly defines the key roles played by finite deformation theory and the bifurcated constitutive model on the prediction of the post-localization responses, a first step has been taken to reach this goal. The fact that the proposed multiscale model does not require static condensation to be performed on the element level is an added attribute of the formulation. Large deformation effects are currently not well understood in strain localization modeling, and although significant strides have been made in the past, progress in the development of more efficient, accurate, and robust procedures remains limited. Although there are several other aspects of the formulation that need more work, such as the development of an efficient band tracing algorithm, it is hoped that this paper, together with its predecessors, will help make finite deformation theory a routine part of strain localization modeling.

Acknowledgements

The author is grateful to Medji Sama and an anonymous reviewer for reading and reviewing this manuscript. The work presented in this paper was supported in part by National Science Foundation under grant no. CMS97-00426.

References

[1] A. Nádai, Plasticity, McGraw-Hill, New York, 1931.
[2] J.W. Hutchinson, K.W. Neale, Neck propagation, J. Mech. Phys. Solids 31 (1983) 405–426.
[3] H.E. Read, G.A. Hegemier, Strain softening of rock, soil and concrete—a review article, Mech. Mater. 3 (1984) 271–294.

[4] P.A. Vermeer, R. de Borst, Nonassociated plasticity for soils, concrete, and rock, Heron 29 (1984) 1–64.
[5] I. Vardoulakis, B. Graf, Calibration of constitutive models for granular materials using data from biaxial experiments, Géotechnique 35 (1985) 299–317.
[6] Z.P. Bazant, J. Planas, Fracture and Size Effect in Concrete and Other Quasibrittle Materials, CRC Press, Boca Raton, FL, 1998.
[7] E. van der Giessen, R. de Borst, Introduction to material instabilities in solids, in: R. de Borst, E. van der Giessen (Eds.), Material Instabilities in Solids, Wiley, New York, 1998, pp. 1–13, Chapter 1.
[8] J. Hadamard, Lecons sur la Propagation des Ondes, Herman, Paris, 1903.
[9] R. Hill, A general theory of uniqueness and stability in elastic–plastic solids, J. Mech. Phys. Solids 10 (1958) 1–16.
[10] Y. Thomas, Plastic Flow and Fracture of Solids, Academic Press, New York, 1961.
[11] J. Mandel, Conditions de stabilité et postulat de Drucker, in: Proceedings IUTAM Symposium on Rheology and Soil Mechanics, Springer, Berlin, 1966, pp. 58–68.
[12] J.R. Rice, The localization of plastic deformation, in: W.T. Koiter (Ed.), Theoretical and Applied Mechanics, North-Holland, Amsterdam, 1976, pp. 207–220.
[13] J.W. Rudnicki, J.R. Rice, Conditions for the localization of deformation in pressure-sensitive dilatant materials, J. Mech. Phys. Solids 23 (1975) 371–394.
[14] D. Kolymbas, Bifurcation analysis for sand samples with a non-linear constitutive equation, Ingenieur-Archiv 50 (1981) 131–140.
[15] J. Desrues, R. Chambon, Shear band analysis for granular materials: the question of incremental non-linearity, Ingenieur-Archiv 59 (1989) 187–196.
[16] R. Chambon, S. Crochepeyre, J. Desrues, Localization criteria for non-linear constitutive equations of geomaterials, Mech. Cohes. Frict. Mater. 5 (2000) 61–82.
[17] C. Tamagnini, G. Viggiani, R. Chambon, Some remarks on shear band analysis in hypoplasticity, in: H.B. Mühlhaus, A.V. Dyskin, A. Pasternak (Eds.), Bifurcation and Localisation Theory in Geomechanics, Balkema, Lisse, The Netherlands, 2001, pp. 85–93.
[18] D. Bigoni, Bifurcation and instability of non-associative elastoplastic solids, in: CISM Lecture Notes on the Course: Material Instabilities in Elastic and Plastic Solids, H. Petryk (Coordinator), Udine, 13–17 September, 1999.
[19] T.J.R. Hughes, Multiscale phenomena: Green's functions, the Dirichlet-to-Neumann formulation, subgrid scale models, bubbles and the origins of stabilized methods, Comput. Meth. Appl. Mech. Engrg. 127 (1995) 387–401.
[20] T.J.R. Hughes, A space-time formulation for multiscale phenomena, J. Comput. Appl. Math 74 (1996) 217–229.
[21] K. Garikipati, T.J.R. Hughes, A study of strain localization in a multiple scale framework—the one-dimensional problem, Comput. Meth. Appl. Mech. Engrg. 159 (1998) 193–222.
[22] K. Garikipati, T.J.R. Hughes, A variational multiscale approach to strain localization—formulation for multidimensional problem, Comput. Meth. Appl. Mech. Engrg. 188 (2000) 39–60.
[23] R.I. Borja, R.A. Regueiro, T.Y. Lai, FE modeling of strain localization in soft rock, J. Geotech. Geoenviron. Engrg. ASCE 126 (2000) 335–343.
[24] R.I. Borja, A finite element model for strain localization analysis of strongly discontinuous fields based on standard Galerkin approximation, Comput. Meth. Appl. Mech. Engrg. 190 (2000) 1529–1549.
[25] R.I. Borja, R.A. Regueiro, Strain localization of frictional materials exhibiting displacement jumps, Comput. Meth. Appl. Mech. Engrg. 190 (2001) 2555–2580.
[26] R.A. Regueiro, R.I. Borja, Plane strain finite element analysis of pressure sensitive plasticity with strong discontinuity, Int. J. Solids Struct. 38 (2001) 3647–3672.
[27] R.I. Borja, T.Y. Lai, Propagation of localization instability under active and passive loading, J. Geotech. Geoenviron. Engrg. ASCE 128 (2002) 64–75.
[28] A. Aydin, Small faults formed as deformation bands in sandstone, PAGEOPH 116 (1978) 913–930.
[29] K.M. Flores, R.H. Dauskardt, Local heating associated with crack tip plasticity in Zr–Ti–Ni–Cu–Be bulk amorphous metals, J. Mater. Res. 14 (1999) 638–643.
[30] R.I. Borja, Bifurcation of elastoplastic solids to shear band mode at finite strain, Comput. Meth. Appl. Mech. Engrg., to appear.
[31] F. Armero, K. Garikipati, An analysis of strong discontinuities in multiplicative finite strain plasticity and their relation with the numerical simulation of strain localization in solids, Int. J. Solids Struct. 33 (1996) 2863–2885.
[32] R. Larsson, P. Steinmann, K. Runesson, Finite element embedded localization band for finite strain plasticity based on a regularized strong discontinuity, Mech. Cohes. Frict. Mater. 4 (1998) 171–194.
[33] J.C. Simo, M.S. Rifai, A class of mixed assumed strain methods and the method of incompatible modes, Int. J. Numer. Meth. Engrg. 29 (1990) 1595–1638.
[34] J.C. Simo, J. Oliver, A new approach to the analysis and simulation of strain softening in solids, in: Z.P. Bazant, et al. (Eds.), Fracture and Damage in Quasibrittle Structures, E&FN Spon, London, 1994, pp. 25–39.
[35] F. Armero, K. Garikipati, Recent advances in the analysis and numerical simulation of strain localization in inelastic solids, in: D.R.J. Owen, E. Oñate, E. Hinton (Eds.), Proceedings of Computational Plasticity, vol. 4, CIMNE, Barcelona, Spain, 1995, pp. 547–561.

[36] R. Larsson, K. Runesson, Discontinuous displacement approximation for capturing plastic localization, Int. J. Numer. Meth. Engrg. 36 (1993) 2087–2105.
[37] R.L. Taylor, J.C. Simo, O.C. Zienkiewicz, A.C.H. Chan, The patch test—a condition for assessing FEM convergence, Int. J. Numer. Meth. Engrg. 22 (1986) 39–62.
[38] R.W. Ogden, Nonlinear Elastic Deformations, Ellis Horwood, Chichester, 1984.
[39] E.H. Lee, Elastic–plastic deformation at finite strains, J. Appl. Mech. (1969) 1–6.
[40] Y.F. Dafalias, Plastic spin: necessity or redundancy?, Int. J. Plasticity 14 (1998) 909–931.
[41] W.A. Olsson, Theoretical and experimental investigation of compaction bands in porous rock, J. Geophys. Res. 104 (1999) 7219–7228.
[42] R.I. Borja, J.R. Wren, Discrete micromechanics of elastoplastic crystals, Int. J. Numer. Meth. Engrg. 36 (1993) 3815–3840.